

# Conditions Under Which Heterogeneous Charge-Transfer Rate Constants Can Be Extracted from Transient Photoluminescence Decay Data of Semiconductor/Liquid Contacts As Determined by Two-Dimensional Transport Modeling

Samir J. Anz, Olaf Krüger,<sup>†</sup> and Nathan S. Lewis\*

Division of Chemistry and Chemical Engineering, California Institute of Technology, Pasadena, California 91125

Herbert Gajewski\*

Weierstrass-Institut, Hausvogteiplatz 5-7, D-10117 Berlin, Germany

Received: December 19, 1997; In Final Form: March 26, 1998

An extensive series of digital simulations of the decay dynamics of photoexcited charge carriers at a semiconductor/liquid interface has been performed using the two-dimensional simulation code ToSCA. ToSCA treats majority and minority carrier capture processes separately and incorporates field-dependent carrier mobility terms. These features produce dramatic differences in the output parameters obtained when fitting experimental data with ToSCA relative to those obtained by fitting such data with prior, less complete, simulations. The simulations revealed that for a typical (n-type in our example) InP electrode in contact with outer-sphere redox reagents dissolved in the liquid phase the photoluminescence decays were generally insensitive to the value of the minority carrier charge-transfer rate constant,  $k_{ht}$ . Instead, diffusion and drift-induced separation of photogenerated carriers in the space-charge layer of the semiconductor dominated the time decay of the observed luminescence signal under most experimentally accessible conditions. Values of  $k_{ht}$  and of the minority carrier low-level surface recombination velocity,  $S_p$ , could be obtained from an analysis of the photoluminescence decays only when the following restricted sets of conditions were satisfied simultaneously:  $10^1 \text{ cm s}^{-1} \leq S_p \leq 10^5 \text{ cm s}^{-1}$ ,  $10^{-18} \text{ cm}^4 \text{ s}^{-1} \leq k_{ht} \leq 10^{-15} \text{ cm}^4 \text{ s}^{-1}$ , and the electrode potential,  $E$ , was in the region  $0 < E < +0.15 \text{ V}$  relative to the flat-band potential of the n-type semiconductor/liquid interface. The simulations demonstrated that it was not possible to extract a “field dependence” of the charge-transfer rate constant when the semiconductor/liquid contact was maintained in reverse bias ( $E \geq +0.15 \text{ V}$  vs the flat-band potential) and was subjected to light pulses that produced low or moderate carrier injection levels. Under such conditions, the photoluminescence decay dynamics were dominated by drift-induced charge separation in the space-charge layer of the semiconductor. Under high-level injection conditions, no “field dependence” could be observed because the majority of the photoluminescence decay dynamics occurred near the flat-band condition, so the value of the band bending in the semiconductor under dark, equilibrium conditions had negligible influence on the luminescence transients produced by a high-intensity laser pulse. Additionally, comparison between one-dimensional and two-dimensional simulations showed that use of one-dimensional simulation routines to extract  $S_p$  and  $k_{ht}$  values from experimental data obtained using focused laser beam excitation can lead to severe overestimates of interfacial charge-transfer rates.

## I. Introduction

Understanding heterogeneous charge-transfer rate constants,  $k_{ct}$ , across semiconductor/liquid interfaces is important in evaluating the factors that control the stability and energy conversion efficiency of photoelectrochemical cells.<sup>1–5</sup> At present, five separate theoretical approaches of various levels of sophistication, ranging from simple classical collision models to a Fermi golden rule based electronic coupling approach, have all predicted values of the rate constant at optimal exoergicity from delocalized charge carriers in a semiconducting solid to localized, nonadsorbed, outer-sphere redox species in solution to be approximately  $10^{-17}$ – $10^{-16} \text{ cm}^4 \text{ s}^{-1}$ .<sup>3,6–13</sup> In addition, several different experimental methods have provided upper bounds on  $k_{ct}$  in various systems of  $k_{ct,max} < 10^{-14} \text{ cm}^4 \text{ s}^{-1}$ ,<sup>7,14,15</sup> and recent direct measurements of  $k_{ct}$  at Si/CH<sub>3</sub>OH and InP/

CH<sub>3</sub>OH contacts have yielded experimental values for  $k_{ct,max}$  of  $10^{-17}$ – $10^{-16} \text{ cm}^4 \text{ s}^{-1}$ .<sup>6,8,12</sup>

Additional measurements of rate constants on systems in which the driving force for electron transfer is smaller than the solvent reorganization energy of the redox couple have yielded values of  $k_{ct}$  in the range of  $10^{-19} \text{ cm}^4 \text{ s}^{-1}$ .<sup>16,17</sup> A recent investigation of GaInP<sub>2</sub>/CH<sub>3</sub>CN contacts has also yielded  $k_{ct}$  values of  $\approx 10^{-17} \text{ cm}^4 \text{ s}^{-1}$  for unetched surfaces, but has provided evidence for  $k_{ct}$  values as large as  $10^{-10} \text{ cm}^4 \text{ s}^{-1}$  for n-GaAs/CH<sub>3</sub>CN junctions under some etching conditions.<sup>18</sup> However, subsequent investigation has indicated that adsorption of the redox acceptor plays a critical role in determining the observed current–potential properties of this particular n-GaAs/liquid contact.<sup>19</sup> Thus, there appears to be good agreement between the theoretical expectations and reported experimental behavior for many well-defined semiconductor/liquid interfaces that do not exhibit strong adsorption effects that have been studied experimentally to date.<sup>20</sup>

\* To whom correspondence should be addressed.

<sup>†</sup> Present address: Institut für Halbleiterphysik, Walter-Korsing-Str. 2, D-15230 Frankfurt(Oder), Germany.

Despite this satisfying agreement between theory and experiment, a model proposed by Gerischer,<sup>10,11</sup> the liquid/liquid electron-transfer theory of Marcus that underlies one of the theoretical models of the semiconductor/liquid contact,<sup>21–23</sup> and the adaptation of this model to semiconductor/liquid interfaces<sup>3,7</sup> have all been criticized recently in the literature.<sup>24,25</sup> Apparently, the doubts concerning some of these prior treatments have been stimulated by two sets of photoluminescence decay measurements at semiconductor/liquid interfaces which have been interpreted to provide evidence for  $k_{ct}$  values much larger than those predicted theoretically, with values of  $k_{ct}$  possibly as large as  $10^{-12} \text{ cm}^4 \text{ s}^{-1}$ .<sup>26,27</sup> These rate constants were deduced from the transient photoluminescence decay data of p-GaAs/CH<sub>3</sub>CN-cobaltocene<sup>+/0</sup> and p-InP/[Fe(CN)<sub>6</sub>]<sup>3–/4–</sup>(aq) interfaces, which were interpreted to indicate that the effective surface recombination velocity had saturated to a value equal to the thermal velocity limit for carriers of  $S_{\text{eff}} = 10^7 \text{ cm s}^{-1}$ . However, a serious confounding factor in the interpretation of the experimental data from these two systems is that these interfaces have recently been shown to involve unstable semiconductor surfaces and/or adsorbed carrier trapping states.<sup>7,28,29</sup> Thus, the measured rate constants for these systems will appear to be artificially large due to either the higher surface recombination velocities associated with the presence of a high density of surface states and/or second-order interfacial kinetic processes resulting from surface oxide formation at these nonideal interfaces. Luminescence decay dynamics that had been assumed to reflect carrier quenching from the direct transfer of charge carriers to nonadsorbed, randomly distributed redox species in the solution phase thus cannot be distinguished from surface recombination processes based on the experimental data available to date.

Additional confounding issues are involved in the interpretation of the bias dependence of the photoluminescence decay signals of p-InP/[Fe(CN)<sub>6</sub>]<sup>3–/4–</sup>(aq) interfaces.<sup>30</sup> In this system, more rapid quenching of the photoluminescence signals as the electrode was biased further into depletion was interpreted to indicate a larger effective minority carrier capture velocity,  $S_{\text{min}}$ , at higher band bending of the electrode.<sup>30,31</sup> Despite the absence of experimental information on the interfacial kinetic rate law that would allow validation of a second-order charge-transfer kinetic process, the “field-dependent”  $S_{\text{min}}$  value obtained from fitting the luminescence decay dynamics to a simulation model was assumed to reflect the rate of carrier transfer to a nonadsorbed, randomly dissolved redox species in the solution phase.<sup>25</sup> The  $S_{\text{min}}$  value deduced at the highest fields was thus divided by the concentration of redox reagent in the bulk of the solution phase,  $c_{\text{red}}$ , to compute a heterogeneous rate constant value of  $k_{ct}$  ( $=S_{\text{min}}/c_{\text{red}}$ ) =  $10^{-12} \text{ cm}^4 \text{ s}^{-1}$  in this system.<sup>24</sup> Furthermore, because the photoluminescence decay simulations produced different values of  $S_{\text{min}}$  at different reverse biases, the experimental behavior was additionally interpreted to provide evidence for a novel, previously unobserved, field dependence of  $k_{ct}$ .<sup>26</sup> Such an interpretation led to the suggestion that the electric field in the semiconductor can accelerate minority carriers to the solid/liquid interface and that the resulting momentum produced by this acceleration could produce very large rate constants for the capture of charge carriers in the solid by acceptor species in the liquid phase.<sup>30,32</sup>

An underlying assumption in the analysis of the data leading to these very large apparent charge-transfer rate constants is that the real-time photoluminescence decay data is sensitive to, and can be used to evaluate quantitatively, the values of  $S_{\text{min}}$  and  $k_{ct}$  for a semiconductor under the experimental conditions of interest. This assumption appears to be in contradiction to

prior experimental work, which has demonstrated that the transient photoluminescence decay signals,<sup>33,34</sup> and the transient photocurrent signals,<sup>35,36</sup> of a strongly depleted semiconductor/liquid interface under low- or moderate-level injection conditions are insensitive to the value of  $k_{ct}$  under most experimentally accessible conditions.

To address these issues, we have performed an extensive series of digital simulations of the decay dynamics of photoexcited charge carriers at a semiconductor/liquid interface using the two-dimensional simulation code ToSCA, which self-consistently solves Poisson’s equation within the van Roosbroeck generation, recombination, and drift-diffusion model.<sup>37,38</sup> The principal intent of performing these simulations was to identify conditions with respect to excitation intensity and applied potential where the rate constants for charge transfer and surface recombination can be unambiguously extracted from experimental photoluminescence decay data. While the steady-state dead-layer model helped pioneer, both pedagogically and quantitatively, the understanding of semiconductor/liquid contacts in general,<sup>34,39</sup> and illuminated semiconductor/liquid contacts in particular,<sup>40–44</sup> this work will summarize the photoluminescence simulations for a semiconductor/liquid contact under transient injection conditions and will reveal significant differences in the fitting of the decay dynamics relative to those produced by earlier models.<sup>30,43–46</sup> The sources of these discrepancies involve the fundamental expressions used to describe the competition between surface recombination and interfacial charge transfer at a solid/liquid interface, as well as factors related to the use of a two-dimensional treatment of the transport and excitation processes in such a system. One of ToSCA’s advantages over other existing simulations is that it treats electron and hole carrier capture processes separately and does not combine them into a single effective surface recombination velocity parameter.<sup>44,47–50</sup> It will be shown that overestimating effective surface recombination velocities can lead to overestimates in interfacial charge-transfer rate constants under many important experimental conditions. The work presented herein therefore provides new insight into, and a useful compilation of simulations for, analysis of photoluminescence decay data at semiconductor/liquid contacts.

## II. Physical Representation of the Semiconductor/Liquid Contact in the Simulation Model

The ToSCA program incorporates a two-dimensional carrier generation profile and utilizes an adaptive triangular spatial lattice to permit computation of the time-dependent carrier concentration profiles in the semiconductor for directions parallel and normal to the plane of the semiconductor/liquid interface. The 32 bit, double-precision simulations were run on an IBM POWERStation 375 workstation and involved minimal computational time. The ToSCA program and its validation with respect to analytical solutions available for several limiting carrier injection and electrode bias combinations have been described in detail previously.<sup>51</sup> For this study, the ToSCA code was extended in several important respects. A trapping model for majority and minority carriers was incorporated to compute explicitly nonradiative recombination via bulk states as well as surface recombination at each bias and trap occupancy level for each time increment of the simulation. Changes in bulk and surface charge due to filling or emptying of these traps were also accounted for in the simulation. The interfacial charge-transfer rates were explicitly treated in terms of the Marcus–Gerischer kinetic formalism, instead of being included implicitly with steady-state surface recombination processes to produce

an effective minority carrier capture velocity.<sup>34,51</sup> Finally, the field dependence of the mobility of electrons in InP was included in the simulation. Each of these modifications is discussed below.

**A. Boundary Conditions.** The choice of boundary conditions is, of course, critical to obtaining a valid simulation for a given system. The boundary conditions used in this work differ significantly from those used in prior studies. This section will therefore discuss these boundary conditions in some detail and compare them with prior boundary condition representations.

*1. Basic Representation of the Boundary Conditions at the Semiconductor/Liquid Contact.* For a semiconductor with a density of surface states (traps) equal to  $N_{t,s}$  (in units of  $\text{cm}^{-2}$ ), where the “s” subscript is used to define a parameter’s surface value, the rate of capture of holes into an electron-occupied surface state is given by

$$\text{hole capture rate} = k_{p,s} N_{t,s} f_i p_s \quad (1)$$

where  $f_i$  is the fraction of states (traps) occupied by electrons,  $p_s$  is the hole concentration (in units of  $\text{cm}^{-3}$ ) at the surface of the semiconductor, and  $k_{p,s}$  is the coefficient for capture of holes (in units of  $\text{cm}^3 \text{s}^{-1}$ ) that defines the rate constant for the hole capture process by surface states. The corresponding rate of emission of holes from surface states unoccupied by electrons into the valence band is

$$\text{hole emission rate} = k_{p,s} N_{t,s} (1 - f_i) p_{1,s} \quad (2)$$

The value of  $p_{1,s}$  is the concentration of holes in the valence band at the surface when the trap energy is at the Fermi energy. The value of  $p_{1,s}$  can be obtained through use of the principle of detailed balance, which when applied to a system at equilibrium in the dark yields<sup>52–54</sup>

$$p_{1,s} = N_v \exp[(E_t - E_v)/kT] \quad (3)$$

where  $k$  is Boltzmann’s constant,  $T$  is the temperature,  $N_v$  is the effective density of states in the valence band,  $E_t$  is the energy of the trap level, and  $E_v$  is the energy of the valence band edge. For the process of emission of holes from traps into the valence band, the product of  $k_{p,s}$  and  $p_{1,s}$  provides the rate constant (in units of  $\text{s}^{-1}$ ).

Using eqs 1 and 2, the net hole flux into surface states is thus

$$\text{net hole flux} = k_{p,s} N_{t,s} f_i p_s - k_{p,s} N_{t,s} (1 - f_i) p_{1,s} \quad (4)$$

An analogous series of equations can likewise be written for the capture and emission rates of electrons at the surface of the solid.

These equations, along with equations for charge transfer across the surface into the solution, are the basis for the boundary conditions used in this work. By including terms that describe the interfacial charge-transfer kinetics, one obtains

$$j_p/q = k_{\text{ht}} c_{\text{red}} (p_s - p_{o,s}) + k_{p,s} N_{t,s} [f_i p_s - (1 - f_i) p_{1,s}] \quad (5)$$

and

$$-j_n/q = k_{\text{et}} c_{\text{ox}} (n_s - n_{o,s}) + k_{n,s} N_{t,s} [(1 - f_i) n_s - f_i n_{1,s}] \quad (6)$$

where eq 6 has a negative sign because cathodic currents are negative by convention.<sup>55</sup> The values of  $j_p$  and  $j_n$  represent the current densities through the valence and conduction bands, respectively,  $q$  is the elementary charge,  $c_{\text{red}}$  and  $c_{\text{ox}}$  are the

concentration of dissolved electron donors and acceptors, respectively, in the electrolyte,  $k_{\text{ht}}$  and  $k_{\text{et}}$  are the rate constants for interfacial charge transfer from the valence and conduction bands of the semiconductor, respectively,  $k_{n,s}$  is the coefficient for capture of electrons by surface states,  $n_s$  is the electron concentration at the semiconductor surface,  $n_{1,s}$  is the concentration of electrons in surface traps, and the subscript “o” is used to indicate a parameter’s value in the dark at equilibrium.

Each capture coefficient is related to the product of the thermal velocity,  $v$ , of the carrier in the solid and the capture cross section,  $\sigma$ , for each kinetic event such that

$$k_{p,s} = v_p \sigma_p \quad \text{and} \quad k_{n,s} = v_n \sigma_n \quad (7)$$

From the principle of detailed balance, it can be shown that the values of  $n_{1,s}$ ,  $p_{1,s}$ ,  $n_1$ , and  $p_1$  are definable as<sup>52–54,56</sup>

$$n_{1,s} = n_{o,s} \exp[(E_f - E_t)/kT]$$

and

$$p_{1,s} = p_{o,s} \exp[(E_t - E_f)/kT] \quad (8a)$$

or, in general, at any point in the solid

$$n_1 = N_c \exp[(E_c - E_t)/kT]$$

and

$$p_1 = N_v \exp[(E_t - E_v)/kT] \quad (8b)$$

where  $N_c$  is the effective density of states in the conduction band,  $E_f$  is the Fermi level energy, and  $E_c$  is the energy of the conduction band. All energies,  $E_c$ ,  $E_v$ , and  $E_f$ , are functions of position in the semiconductor.<sup>33,45,51,57–59</sup>

Equation 5 thus indicates that holes can transfer to redox donors in the solution with a rate constant  $k_{\text{ht}}$  and to filled trap states at the surface with a rate constant  $k_{p,s}$ . Equation 6 is the analogous expression for electrons. In both cases, detailed balance and microscopic reversibility principles can be used to obtain the relationships of eqs 5–8 from elementary kinetic relationships in a straightforward, conventional fashion.<sup>53,57,60,61</sup>

*2. Steady-State vs Dynamic Representation of the Boundary Conditions.* It is useful to compare and contrast the dynamic trapping model presented above with simplifications based on steady-state treatments of surface and bulk carrier recombination dynamics. Under steady-state surface recombination conditions, the net hole and electron fluxes are equal:

$$k_{p,s} N_{t,s} f_i p_s - k_{p,s} N_{t,s} (1 - f_i) p_{1,s} = k_{n,s} N_{t,s} (1 - f_i) n_s - k_{n,s} N_{t,s} f_i n_{1,s} \quad (9)$$

After algebraic manipulation, this expression yields a value for the fractional trap occupancy,  $f_i$ , of

$$f_i = \frac{k_{p,s} p_1 + k_{n,s} n_s}{k_{n,s} (n_s + n_1) + k_{p,s} (p_s + p_1)} \quad (10)$$

Using this expression for  $f_i$ , eq 5 becomes

$$j_p/q = k_{\text{ht}} c_{\text{red}} (p_s - p_{o,s}) + N_{t,s} \frac{k_{p,s} k_{n,s} (n_s p_s - n_1^2)}{k_{n,s} (n_s + n_1) + k_{p,s} (p_s + p_1)} \quad (11)$$

where  $n_i$  is the intrinsic carrier concentration in the undoped

semiconductor. A similar equation can likewise be derived to describe the current density for electrons.

The first term in eq 11 is the rate of interfacial charge-transfer kinetic events. The second term is the rate of Shockley–Read–Hall (SRH) trapping at a semiconductor surface, which is conventionally written as<sup>53,54,56,60,62</sup>

$$R_{\text{SRH}}(\text{Surface}) = \frac{n_s p_s - n_i^2}{\frac{(n_s + n_{1,s})}{N_{t,s} k_{p,s}} + \frac{(p_s + p_{1,s})}{N_{t,s} k_{n,s}}} \quad (12)$$

The Shockley–Read–Hall recombination rate describing the trapping kinetics in the bulk of the semiconductor has a form similar to eq 12, but incorporates parameters that describe the carrier concentrations and trapping rate constants in the bulk of the solid. Equations similar to eqs 10–12 have been used previously to provide boundary conditions for the simulation of photoluminescence decay data using ToSCA.<sup>33,38,51,63</sup> Such steady-state equations do not, however, adequately describe the photoluminescence decay dynamics under all of the conditions of concern in this study. Under steady-state conditions, that is, when the lifetime for the change of trap occupancy is small compared to all other electrical and thermal carrier generation and capture processes, the steady-state Shockley–Read–Hall treatment provides an accurate description of the recombination kinetics for both carrier types with respect to midgap recombination sites.<sup>52–54,58,64</sup> However, in circumstances where the carrier concentration changes rapidly, the SRH model is no longer justifiable because the trap states can become saturated.<sup>52,57</sup> In addition, the SRH model will not be valid when trap occupancy favors one carrier over another.<sup>52</sup> This situation is likely to occur at the surface in the presence of the semiconductor's space-charge layer because the electron and hole concentrations at the surface can differ from each other by many orders of magnitude. This situation might also occur if the trap-state energetics favor capture of one carrier type relative to the other. These situations are also of concern in experiments performed using high excitation intensities or short time-duration laser excitation pulses. Thus, a time-dependent description of the trapping processes, in accord with the kinetic equations of eqs 1–8, is required.<sup>65</sup>

3. *Dynamic Trapping Model (via Separation of Charge-Transfer and Surface Recombination) vs an Effective Minority Carrier Capture Velocity Model.* We note that the boundary conditions of eqs 5–6 differ in several critical respects from the boundary conditions used in photoluminescence decay simulations performed previously.<sup>26,30,45</sup> Prior simulations utilized simplifications of the steady-state SRH boundary conditions, described above, casting them into the form

$$j_p/q = k_{\text{ht}} c_{\text{red}}(p_s - p_{o,s}) + S_p(p_s - p_{o,s}) \quad (13)$$

$$-j_n/q = k_{\text{et}} c_{\text{ox}}(n_s - n_{o,s}) + S_n(n_s - n_{o,s}) \quad (14)$$

where  $S_p$  and  $S_n$  describe the effective overall hole and electron surface recombination velocities, respectively. These steady-state relationships were, in turn, additionally simplified to<sup>30</sup>

$$j_p/q = S_{p,\text{eff}}(p_s - p_{o,s}) \quad \text{with} \quad S_{p,\text{eff}} \equiv k_{\text{ht}} c_{\text{red}} + S_p \quad (15)$$

$$-j_n/q = S_{n,\text{eff}}(n_s - n_{o,s}) \quad \text{with} \quad S_{n,\text{eff}} \equiv k_{\text{et}} c_{\text{ox}} + S_n \quad (16)$$

It was further assumed in some prior work that the recombination rate constants of electrons and holes were identical, such

that<sup>30</sup>

$$S_{n,\text{eff}} = S_{p,\text{eff}} \equiv S \quad (17)$$

In this formalism, the constant  $S$  was the single simulation parameter used to characterize minority carrier capture at the semiconductor/liquid contact for a variety of electrode biases and carrier injection levels, regardless of the individual values of  $k_{\text{ht}}$ ,  $k_{\text{et}}$ ,  $k_{p,s}$ ,  $k_{n,s}$ ,  $N_{t,s}$ , or  $E_t$ .<sup>31</sup>

Implied in eqs 15 and 16 is that both the minority carrier surface recombination rate and the minority carrier charge-transfer rate increase with increasing reverse bias, and thus with increasing value of  $p_s$ . However, surface recombination requires the presence of both electrons and holes at the surface, so the surface recombination rate should decrease as a sample is driven further into reverse bias.<sup>53,56,66</sup> This effect occurs physically because the electric field in the n-type semiconductor space-charge layer will favor localization of minority carriers on the surface while repelling majority carriers into the bulk. In contrast, the rate of interfacial charge transfer increases as the surface concentration of that carrier is increased. Thus, only the rate of minority carrier charge transfer should increase with increasing reverse bias. The use of eqs 15 and 16 combined with the simplification of eq 17 will therefore incorrectly require much larger values of  $k_{\text{ht}}$  to fit experimental data under reverse bias unless artificially large surface recombination rates are allowed to dominate the minority carrier capture velocity of the semiconductor.

**B. The Trap Model for Bulk Recombination and Surface Recombination.** As discussed above, the nonradiative recombination processes were computed for each carrier type at each time increment in the simulation. The traps in the simulation were located in the bulk as well as at the surface and were considered to be situated energetically deep in the band gap and thus thermally un-ionized. Electron and hole capture processes were treated separately at all positions in the bulk and surface of the solid. Equation 4 and an equivalent equation for electrons were used to describe the trapping dynamics at each point in the bulk of the semiconductor.

The traps were either acceptor-like states with a negative or zero charge (depending on their occupancy) or donor-like states with either a zero or positive charge (again depending on their occupancy). Each trap level has two independent capture coefficients, one for electrons and another for holes.<sup>49</sup>

The fundamental differential equation system consisting of Poisson's equation and the continuity equations was extended to incorporate effects that might arise from the time-dependent accumulation of charge in these deep traps.<sup>57,65,67</sup> The equations used for acceptor-like (a) traps were therefore<sup>49</sup>

$$-\nabla(\epsilon \epsilon_0 \nabla U) = N_D^+ + p - n + N_{t,d} f_{t,d} - N_{t,a} f_{t,a} \quad (18)$$

$$dn/dt - \nabla J_n = G + R + N_{t,a} k_n [f_{t,a} n_1 - (1 - f_{t,a}) n] \quad (19)$$

$$dp/dt + \nabla J_p = G + R + N_{t,a} k_p [(1 - f_{t,a}) p_1 - f_{t,a} p] \quad (20)$$

$$df_{t,a}/dt + z f_{t,a} = z f_t \quad (21)$$

where the following relations have been used:

$$z = k_n(n + n_1) + k_p(p + p_1) \quad (22)$$

$$f_t = 0.5 \left\{ 1 + \frac{k_n(n - n_1) + k_p(p - p_1)}{z} \right\} \quad (23)$$



In these equations,  $U$  is the electrostatic potential in the semiconductor,  $N_D^+$  is the concentration of ionized dopant atoms,  $G$  is the Beer–Lambert optical generation function, and  $R$  is the total recombination rate associated with recombination processes other than recombination via the trap model, such as optical and Auger recombinations.<sup>57</sup> All other variables are as defined in eqs 7 and 8, except that in eqs 18–21 they denote either bulk or surface parameters, depending on the location of the traps, hence the elimination of the subscript “s”. A similar set of equations was used to describe donor-like (d) traps.

For stationary conditions,  $df_{t,a}/dt = 0$ , and the rate of carrier capture into the states equals the recombination rate plus the rate of their emission from these states. By defining the bulk nonradiative lifetimes as  $\tau_{0,n} = (N_t k_n)^{-1}$  and  $\tau_{0,p} = (N_t k_p)^{-1}$  and low-level surface recombination velocities as  $S_n = N_{t,s} k_{n,s}$  and  $S_p = N_{t,s} k_{p,s}$ , the generalized trap model simplifies (as it should) to the well-known Shockley–Read–Hall model under steady-state conditions.<sup>52,58,68</sup> These equations thus accurately describe the recombination dynamics as well as the steady-state recombination rates of the system.

**C. The Interfacial Charge-Transfer Model.** Another significant feature of the boundary conditions in our simulation involves the description of the interfacial charge-transfer kinetics. Modifying the boundary conditions at the simulated gate (front) contact of the sample in ToSCA, heterogeneous charge-transfer events were incorporated separately for majority and minority carriers, as follows:<sup>4,50,69</sup>

$$j_c/q = -k_{c,\max} N_c c_{\text{red}} \exp\left[\frac{-(E_c - E_{\text{redox}}^o + \lambda)^2}{4kT\lambda}\right] \left(\frac{n_s}{n_{o,s}} - 1\right) \quad (24)$$

$$j_v/q = k_{v,\max} N_v c_{\text{ox}} \exp\left[\frac{-(E_v - E_{\text{redox}}^o - \lambda)^2}{4kT\lambda}\right] \left(\frac{p_s}{p_{o,s}} - 1\right) \quad (25)$$

In these expressions, the rate constants  $k_{c,\max}$  and  $k_{v,\max}$  are respectively the conduction and valence band charge-transfer rate constants at optimal exoergicity. The redox species forms a redox couple having a formal electrochemical potential of  $E_{\text{redox}}^o$  and a reorganization energy denoted by  $\lambda$ .<sup>4,20,69</sup>

In eq 25, the hole-transfer rate (minority carriers in this study) is not a function of the electron concentration (majority carriers) at the solid/liquid interface. Also, eq 25 correctly predicts that the current via the valence band decreases on going from reverse bias toward flat band, because  $p_s$  (the minority carrier surface concentration in this study) decreases with decreasing band bending. Similar arguments can be used to verify the validity of the equations describing the kinetics of the majority carrier process.

The interfacial charge-transfer rate constants were treated as being independent of the value of the field in the space-charge region of the semiconductor. This was done because we wished to ascertain whether, in fact, experimental photoluminescence decay data provide evidence for invalidating this traditional assumption. Given that carriers undergo thermal excitation to a scattering-limited velocity of  $10^7$  cm s<sup>−1</sup> toward the semiconductor/liquid interface<sup>56</sup> and given that the electric field in the solid only adds direction, but not significant magnitude, to this scattering-limited carrier velocity, it did not seem reasonable to incorporate such an effect into the simulation at the present stage of our understanding of the factors that control carrier transport in semiconducting solids. Further, for a random

distribution of redox species in the solution, since the mean-free-path for electrons in a liquid electrolyte is less than a few angstroms,<sup>55</sup> any excess thermal velocity of a ballistically ejected charge carrier (if such existed under the simulated experimental conditions) would be rapidly dissipated before the charge carrier could encounter many of the redox sites that participate in the heterogeneous charge-transfer event.

**D. Mobility Model.** In ToSCA, the driving forces for carriers to move in the semiconductor are the gradients of the quasi-Fermi levels for electrons and holes,  $E_{F,n}$  and  $E_{F,p}$ , respectively.<sup>56</sup> The resulting position-dependent electron and hole current densities,  $J_n$  and  $J_p$ , are proportional to the electron and hole mobilities,  $\mu_n$  and  $\mu_p$ , respectively, and can be calculated as follows:

$$J_n = -qn\mu_n \nabla E_{F,n} \quad (26)$$

$$J_p = qp\mu_p \nabla E_{F,p} \quad (27)$$

The thermal limit on the velocity of charge carriers in a semiconductor is  $\approx 10^7$  cm s<sup>−1</sup>.<sup>56</sup> To first order, the carrier drift velocity is the product of the mobility and the electric field component in the direction of current flow. Under the influence of increasingly large electric fields, these carrier drift velocities must saturate to this thermal limit. Recently, several models have been advanced to describe the influence of high electric fields on the carrier mobilities of Si and GaAs.<sup>70</sup> To our knowledge, an equation describing the dependence of the drift velocity on the electric field for InP is not available in the literature. However, a recently published comparison between Monte Carlo simulations and experimental data on electron transport in GaAs and InP showed that these two semiconductors display very similar carrier transport processes.<sup>71</sup> The GaAs mobility model was thus adapted to the InP system, yielding<sup>70,72</sup>

$$\mu_n = \frac{\mu_{o,n} + v_{\text{sat},n} \frac{\mathcal{E}^2}{\mathcal{E}_{\text{crit}}^4}}{1 + \left(\frac{\mathcal{E}}{\mathcal{E}_{\text{crit}}}\right)^4} \quad (28)$$

In eq 28,  $\mathcal{E}$  denotes the electric field strength,  $\mathcal{E}_{\text{crit}}$  is the critical field strength,  $\mu_{o,n}$  denotes the zero-field mobility of the electrons, and  $v_{\text{sat},n}$  represents the saturation velocity of electrons in the presence of large electric fields.

Although ToSCA can be used to compute the dependence of the mobilities on temperature and doping concentration, the experimental values for the room-temperature low-field electron mobility of InP published by Majerfeld et al. of  $\mu_{o,n} = 3600$  cm<sup>2</sup> V<sup>−1</sup> s<sup>−1</sup> for a carrier concentration of  $n_o = 9.7 \times 10^{14}$  cm<sup>−3</sup> were input explicitly in the simulation routine.<sup>73</sup> Using  $v_{\text{sat},n} = 8.5 \times 10^6$  cm s<sup>−1</sup> and  $\mathcal{E}_{\text{crit}} = 12$  kV cm<sup>−1</sup>, a peak velocity of  $2.7 \times 10^7$  cm s<sup>−1</sup> at an electric field of  $10$  kV cm<sup>−1</sup> was obtained. This value agrees well with experimental measurements as well as with recent simulations.<sup>71,73–76</sup> Experimentally, electric fields of sufficient magnitude to require electron velocities to be saturated in n-InP can be realized for moderately doped samples at bias potentials as small as  $0.15$  V positive of the flat-band potential.

In contrast to the treatment of electrons in InP, the mobility of holes was not limited. This is justified because in InP, holes are less mobile than electrons. Assuming a hole mobility of  $150$  cm<sup>2</sup> V<sup>−1</sup> s<sup>−1</sup> at room temperature, as measured by Siegel et al. for a p-type InP sample having a hole concentration of  $p_o \approx 4 \times 10^{16}$  cm<sup>−3</sup>, holes will reach their thermal velocity limit

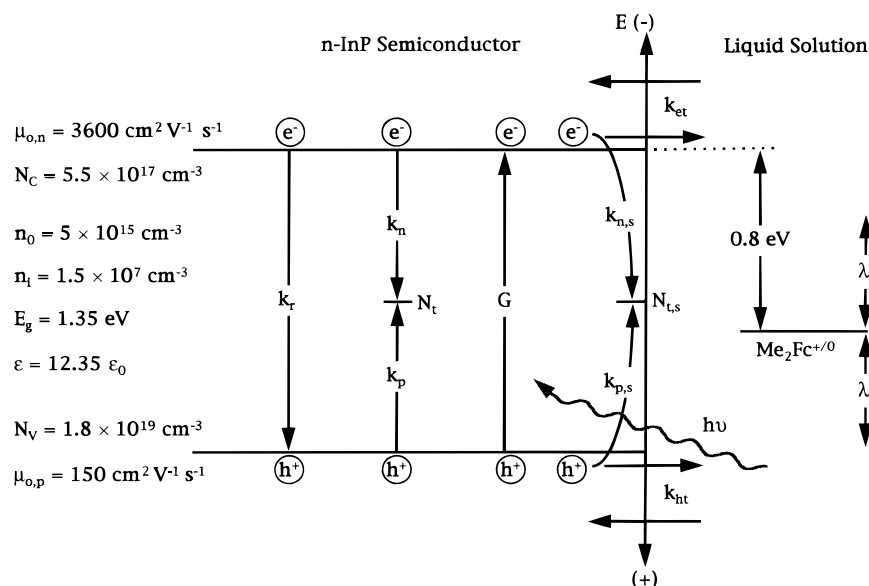


**Figure 1.** Schematic of the n-InP system used in our simulation. The various carrier recombination mechanisms and the quantitative values for the parameters required for the simulations are illustrated. The sample's band-gap energy,  $E_g$ , was 1.35 eV, the intrinsic carrier concentration,  $n_i$ , was  $1.5 \times 10^7 \text{ cm}^{-3}$ ,  $\epsilon$  is the dielectric constant of the electrode, and  $\epsilon_0$  is the permittivity of the vacuum. The junction's barrier height was 0.8 V; that is, the solution's redox potential was 0.8 V below the conduction band edge at the surface, and the reorganization energy of the redox species in solution was held constant at  $\lambda = 0.5 \text{ eV}$ .

at an electric field of about  $100 \text{ kV cm}^{-1}$ .<sup>76,77</sup> This value is well out of the regimes encountered by our present simulations and is expected to be encountered experimentally only for biases greater than  $E = 1.1 \text{ V}$  vs the flat-band potential.

**E. Simulation Parameters.** Figure 1 schematically illustrates the n-InP system (doping concentration  $n_o = 5 \times 10^{15} \text{ cm}^{-3}$ ) and the quantitative values for the intensive parameters used in the simulation. The trap states were set to have donor-like character, i.e., zero charge when occupied with electrons and positively charged when empty. The rate constant for radiative recombination in the bulk of the semiconductor was set at  $k_r = 2 \times 10^{-10} \text{ cm}^3 \text{ s}^{-1}$ ,<sup>76</sup> and the bulk ( $k_n$  and  $k_p$ ) and surface ( $k_{n,s}$  and  $k_{p,s}$ ) capture coefficients were set at  $10^{-8} \text{ cm}^3 \text{ s}^{-1}$ .<sup>76</sup> The density of recombination sites in the bulk of the crystal was set to  $N_t = 10^{15} \text{ cm}^{-3}$ . This value yielded a low-level minority carrier lifetime of 100 ns, in good agreement with experimental data on n-InP samples.<sup>76,77</sup> The concentrations of both the oxidized and reduced forms of the redox species, 1,1'-dimethylferrocene<sup>+/0</sup>, were set to 0.10 M. The formal potential of the redox couple was 0.8 V from the conduction band, and the reorganization energy was held constant at  $\lambda = 0.5 \text{ eV}$ .<sup>6,8,78</sup>

The simulated laser pulse had a maximum intensity at 200 ps and a full width at half-maximum (fwhm) value of 70 ps. The fwhm was set to 70 ps to simulate the entire system response in a time-resolved single-photon-counting experiment and to avoid having to convolute the simulated photoluminescence decay transients from a 6 ps pulse emanating from a mode-locked, dye-pumped Nd:YAG laser with the system response function. Simulations using shorter pulses validated this procedure in a selection of test cases. The incident light had a wavelength of 670 nm. The absorption coefficient for InP at this wavelength is  $\alpha = 5.9 \times 10^4 \text{ cm}^{-1}$ ,<sup>76</sup> and the resulting penetration depth ( $\alpha^{-1}$ ) is  $0.17 \mu\text{m}$ . The simulated sample was  $200 \mu\text{m}$  thick ( $x$ -dimension) and  $0.1 \mu\text{m}$  wide ( $y$ -dimension). The electrode surface was  $100 \mu\text{m} \times 0.1 \mu\text{m}$  in area and was illuminated uniformly except when indicated otherwise. Because ToSCA is a two-dimensional simulation program, the sample was considered to be uniform in the  $z$ -direction (height

$= 100 \mu\text{m}$ ). The boundary conditions at the edges of the  $0.1 \mu\text{m}$  wide simulated slice were set such that zero flux and zero recombination occurred at the boundaries. Thus, in essence, except where indicated otherwise, the simulations describe the situation for a sample that is  $200 \mu\text{m}$  thick and is of infinite width and height (i.e., a quasi one-dimensional simulation). Since the ToSCA code was originally designed to simulate the behavior of solid-state electronic devices, ToSCA was adapted to the situation for a semiconductor/liquid contact by using a modified (leaky) gate contact with the gate "oxide" having the properties of a Helmholtz double layer, that is, a thickness of  $0.3 \text{ nm}$  and a dielectric constant of  $\epsilon_H = 6\epsilon_0$ .<sup>55</sup>

Four key experimental parameters were varied in the simulations: the injection level, the electrode potential, the surface trap density, and the minority carrier charge-transfer rate constant at optimal exoergicity. The carrier injection level, defined as the average density of photogenerated minority carriers,  $p_i$ , injected within the light penetration depth ( $\alpha^{-1}$ ) divided by the equilibrium doping concentration in the semiconductor,  $n_o$ , was an input parameter that was varied from  $p_i/n_o = 10^{-6}$  to  $p_i/n_o = 10$  to explore a range of injection levels that might be attained experimentally. The back (ohmic) contact bias was varied to produce potentials,  $E$ , across the semiconductor of 0, 0.05, 0.10, and 0.15 V relative to the flat-band potential,  $E_{fb}$ , of the semiconductor/liquid interface. The density of surface states was varied from  $10^9$  to  $10^{15} \text{ cm}^{-2}$ , yielding low-level minority carrier surface recombination velocities,  $S_p$ , of  $10^1$ – $10^7 \text{ cm s}^{-1}$ , respectively. In the work presented here, the individual low-level surface recombination rates for holes and electrons were equal ( $S_n = S_p$ ). To facilitate comparison to prior work, the value of  $S_p$  was used to index the various simulations presented herein, but in our simulations  $S_p$  was not an input variable; it only indicated the value of  $N_{t,s}$  used in the surface trapping model for that specific simulation. Finally, the value of the charge-transfer rate constant at optimal exoergicity (maximum charge-transfer rate constant) was varied from  $10^{-18}$  to  $10^{-13} \text{ cm}^4 \text{ s}^{-1}$ . As will be described below, increases in  $k_{v,max}$  above  $10^{-15} \text{ cm}^4 \text{ s}^{-1}$  had essentially no effect on the simulated photoluminescence decays in almost all regions of experimental

interest, so larger  $k_{v,\max}$  were not further explored. Using eqs 24 and 25, at  $k_{c,\max} = k_{v,\max} = 10^{-16} \text{ cm}^4 \text{ s}^{-1}$  and  $c_{\text{ox}} = c_{\text{red}} = 0.1 \text{ M}$ , these parameters yielded effective interfacial electron and hole transfer velocities of  $1.1 \times 10^3$  and  $5.7 \times 10^3 \text{ cm s}^{-1}$ , respectively. Interfacial charge transfer between the redox species and both bands was explicitly considered in all of the simulations, but only the minority carrier charge-transfer rate constants,  $k_{\text{ht}}$ , are depicted in the figures and in the related discussions. The parameters  $k_{\text{ht}}$  and  $k_{\text{et}}$  can be related to  $k_{v,\max}$  and  $k_{c,\max}$  using eqs 24 and 25 with  $k_{v,\max} = k_{c,\max}$  and the appropriate values of  $\lambda$  and  $\mathbf{E}_c - \mathbf{E}_{\text{redox}}^0$ . With our system, these parameters yielded a minority carrier charge-transfer rate constant,  $k_{\text{ht}}$ , within 95% of the value of  $k_{v,\max}$ .

**F. Comparison between Simulations and Analytical Solutions in Certain Limiting Cases.** Several simulations were performed using initial conditions and boundary conditions for which analytical solutions are available. These comparisons validated individually the generation, diffusion, bulk recombination, and surface recombination aspects of the code. Specifically, the simulations validated the Beer's law generation function, Fickian diffusion behavior of charge carriers in the bulk of the solid, the surface recombination kinetics of charge carriers under low-level and high-level injection in the bulk and at the surface of the semiconductor, and radiative recombination processes in the bulk of the solid. In addition, simulations produced agreement with the Vaitkus model<sup>57,79–81</sup> and with the SRH surface recombination models under conditions where these models were applicable.<sup>51,57</sup> These validation runs are included in the Supporting Information that accompanies this article.

**G. Data Analysis.** Although the simulated photoluminescence transients are not in general exponential in nature, for tabulation purposes the simulated spectra were fit, for simplicity, to a biexponential form:

$$I_{\text{PL}}(t) = A_1 \exp(-t/\tau_1) + A_2 \exp(-t/\tau_2) \quad (29)$$

The fit was performed from the time of the peak photoluminescence intensity to the time at which the photoluminescence signal had decayed to 1% of its peak value. Each fit was described by an effective lifetime value,  $\langle\tau\rangle$ , that was computed using the following relationship:

$$\langle\tau\rangle = \frac{A_1\tau_1 + A_2\tau_2}{A_1 + A_2} \quad (30)$$

where  $A_1$  and  $A_2$  are the preexponential factors,  $\tau_1$  and  $\tau_2$  are the exponential decay times of the fit (eq 29), and  $\langle\tau\rangle$  is the effective lifetime of the photoluminescence signal. In contrast to previous fitting procedures used for other simulations,<sup>80</sup> our  $\langle\tau\rangle$  values contain terms that are linear rather than quadratic with respect to these decay times,  $\tau_n$ . Equation 30 does not bias a  $\langle\tau\rangle$  value toward the longer of the two decay times derived from the fitting procedure. This is especially important at high  $N_{\text{ts}}$  values or at large  $k_{\text{ht}}$  values, because the surface concentration of carriers can be rapidly reduced, initiating a fast photoluminescence decay for a short time duration, followed by a slower photoluminescence decay as bulk carriers recombine.

### III. Simulation Results

**A. High-Level Injection Simulations at the Flat-Band Potential.** To investigate high-level injection conditions, photoluminescence transients were simulated at an injection level

of  $p_i/n_o = 10$ . After such an intense injection pulse in a short time period, the equilibrium electric field in the semiconductor is virtually eliminated by the presence of a high concentration of both minority and majority free carriers near the surface.<sup>27,35,51,82,83</sup>

Figures 2a–d illustrate the simulated photoluminescence decay dynamics for a range of different values of  $k_{\text{ht}}$  as a function of the surface state density,  $N_{\text{ts}}$ . Four different  $N_{\text{ts}}$  values were used, ranging from  $10^9$  to  $10^{15} \text{ cm}^{-2}$ , to produce corresponding low-level minority carrier surface recombination velocities,  $S_p$ , ranging from  $10^1$  to  $10^7 \text{ cm s}^{-1}$ . At each value of  $N_{\text{ts}}$ , the photoluminescence decay dynamics asymptotically approached two limiting decay forms, one form for long lifetimes (low  $k_{\text{ht}}$  values) and one form for short lifetimes (high  $k_{\text{ht}}$  values). For instance, as displayed in Figure 2a, for  $N_{\text{ts}} = 10^9 \text{ cm}^{-2}$  ( $S_p = 10^1 \text{ cm s}^{-1}$ ) little change in the photoluminescence decay was observed when  $k_{\text{ht}}$  was decreased from  $10^{-17} \text{ cm}^4 \text{ s}^{-1}$  ( $5.7 \times 10^2 \text{ cm s}^{-1}$  effective transfer velocity) to  $10^{-18} \text{ cm}^4 \text{ s}^{-1}$  ( $5.7 \times 10^1 \text{ cm s}^{-1}$  effective transfer velocity). Further decreases in  $k_{\text{ht}}$  below this value produced essentially no change in the long-lifetime asymptotic photoluminescence decay form. Similarly, for  $N_{\text{ts}} = 10^9 \text{ cm}^{-2}$ , the decays for  $k_{\text{ht}} = 10^{-14} \text{ cm}^4 \text{ s}^{-1}$  ( $5.7 \times 10^5 \text{ cm s}^{-1}$  effective transfer velocity) were essentially identical to those predicted for  $k_{\text{ht}} = 10^{-13} \text{ cm}^4 \text{ s}^{-1}$ , or for any higher value of  $k_{\text{ht}}$  under these conditions. These transients thus represent the short-lifetime asymptote at  $p_i/n_o = 10$  for this particular set of variables.

The variation in the photoluminescence decay dynamics separating the two differently asymptotic decay forms narrowed as  $N_{\text{ts}}$  increased (Table 1). For example,  $k_{\text{ht}}$  values between  $10^{-17}$  and  $10^{-14} \text{ cm}^4 \text{ s}^{-1}$  could clearly be differentiated at  $N_{\text{ts}} = 10^9 \text{ cm}^{-2}$  (Figure 2a), whereas for  $N_{\text{ts}} = 10^{13} \text{ cm}^{-2}$  only  $k_{\text{ht}} = 10^{-15}$  and  $10^{-14} \text{ cm}^4 \text{ s}^{-1}$  could be distinguished by analysis of the photoluminescence decay transients (Figure 2c). For  $N_{\text{ts}} = 10^{15} \text{ cm}^{-2}$  ( $S_p = 10^7 \text{ cm s}^{-1}$ ), the range of  $k_{\text{ht}}$  values contained between the short- and long-lifetime photoluminescence asymptotic forms is so small that it would be extremely difficult to extract accurate  $k_{\text{ht}}$  values from the experimental photoluminescence decay data of such systems.

The behavior depicted in the simulations of Figure 2 can be understood by considering the carrier transport and recombination dynamics under high-level injection. The excitation pulse produces an exponential concentration profile of injected carriers, so the luminescence is initially very intense because it involves second-order recombination between electrons and holes created in the same region of the solid.<sup>57,58</sup> Diffusional motion of carriers tends to alleviate this carrier concentration gradient and therefore eventually eliminates the quadratic recombination to yield a simple, exponentially decaying photoluminescence signal. In the limit of negligible nonradiative recombination, the long-lifetime photoluminescence decay asymptote is determined solely by the carrier mobilities, the optical penetration depth, and the carrier injection level used in the experiment. An approximation of this condition is depicted in Figure 2a for  $k_{\text{ht}} = 10^{-18} \text{ cm}^4 \text{ s}^{-1}$ .

The short-lifetime photoluminescence decay asymptote can also be readily understood. When carriers are removed non-radiatively from the solid as fast as they arrive at the solid/liquid interface, either by surface recombination or by interfacial charge-transfer processes (or a combination thereof), the photoluminescence decay will reach a short-lifetime asymptote. Any additional increases in  $k_{\text{ht}}$  or  $N_{\text{ts}}$  cannot affect the photoluminescence decay dynamics because the carrier quenching is already limited by diffusion of carriers to the surface. Thus,

$$E - E_{\text{fb}} = 0.0 \text{ V}, \quad p_i/n_o = 10$$

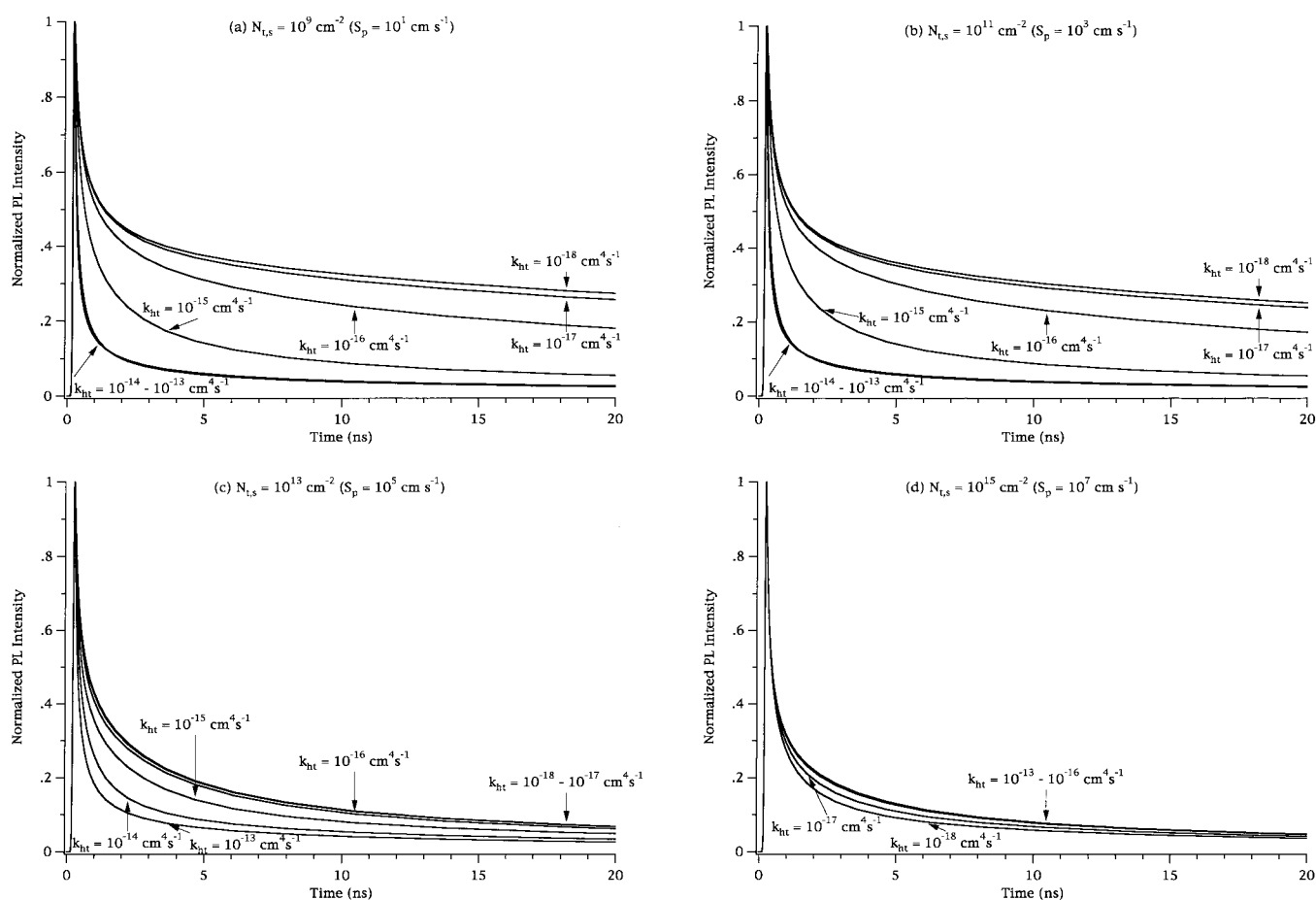


**Figure 2.** Simulated photoluminescence transients under flat-band potential conditions at the high injection level ( $p_i/n_o$ ) of 10. The influence of  $k_{\text{ht}}$  on photoluminescence decays is illustrated for  $N_{\text{t,s}}$  ( $S_p$ ) values of (a)  $10^9$  ( $10$ ), (b)  $10^{11}$  ( $10^3$ ), (c)  $10^{13}$  ( $10^5$ ), and (d)  $10^{15}$  ( $10^7$ )  $\text{cm}^{-2}$  ( $\text{cm s}^{-1}$ ).

like the long-lifetime photoluminescence decay asymptote, the short-lifetime photoluminescence decay asymptote is determined entirely by the carrier mobilities, the optical penetration depth, and the carrier injection level used in the experiment. An example of this asymptote can be seen in Figure 2a for  $k_{\text{ht}} \geq 10^{-14} \text{ cm}^4 \text{ s}^{-1}$  or in the most rapid decay transients of any of the other panels of Figure 2.

This set of physical limits on the photoluminescence decays suffices to explain all of the qualitative trends observed in the simulations of Figure 2. As  $N_{\text{t,s}}$  is increased, nonradiative surface recombination will occur more rapidly even at the lowest  $k_{\text{ht}}$  values, so the decay time of the long-lifetime asymptote will shorten (cf. simulations for  $k_{\text{ht}} = 10^{-18} \text{ cm}^4 \text{ s}^{-1}$  for different  $N_{\text{t,s}}$  values in Figures 2a–d). The range between the long-lifetime and short-lifetime  $k_{\text{ht}}$  asymptotes will therefore narrow at higher  $N_{\text{t,s}}$  values, in accord with the simulations of Figures 2a–d.

At the highest  $N_{\text{t,s}}$  values, a subtle effect can be seen through careful comparison of the photoluminescence decay simulations. The decays at  $N_{\text{t,s}} = 10^{15} \text{ cm}^{-2}$  ( $S = 10^7 \text{ cm s}^{-1}$ ) and  $k_{\text{ht}} \geq 10^{-14} \text{ cm}^4 \text{ s}^{-1}$  (Figure 2d) are actually slightly longer-lived than those at  $N_{\text{t,s}} = 10^{13} \text{ cm}^{-2}$  ( $S = 10^5 \text{ cm s}^{-1}$ ) and  $k_{\text{ht}} \geq 10^{-15} \text{ cm}^4 \text{ s}^{-1}$  (Figure 2c), because the higher rate of surface recombination for  $N_{\text{t,s}} = 10^{15} \text{ cm}^{-2}$  rapidly removes carriers near where they are initially created and thus competes more effectively with the initial second-order decay process at the earliest times after the injection pulse. The decays after this early time period are, however, extremely similar, and it would thus be very difficult to distinguish between these two sets of conditions based on an analysis of experimental photoluminescence decay data.

**B. Low-Level Injection Simulations at the Flat-Band Potential.** A somewhat different situation is observed in simulations carried out under low-level injection conditions. The following simulations utilized an injection level  $p_i/n_o = 10^{-6}$ , but nearly identical results were observed for any injection level of  $p_i/n_o < 10^{-1}$ .

Figures 3a–d show the simulated photoluminescence transients at the flat-band condition under these injection conditions. Simulations performed using various values of  $k_{\text{ht}}$ , ranging from  $10^{-18}$  to  $10^{-13} \text{ cm}^4 \text{ s}^{-1}$ , are plotted for fixed values of  $N_{\text{t,s}}$  between  $10^9$  and  $10^{15} \text{ cm}^{-2}$ . As observed in the high-level injection simulations, for each value of  $N_{\text{t,s}}$  the photoluminescence decays exhibited two asymptotic forms, one form having a long lifetime and the other having a short lifetime. Another similarity is the narrowing of the region over which the photoluminescence decays are sensitive to  $k_{\text{ht}}$  as  $N_{\text{t,s}}$  is increased and other parameters are held constant (cf. Figures 3a–d).

The behavior at  $E = 0$  is readily understood on the basis of the concepts discussed in section III.A. In the low-level injection limit, the majority carrier concentration in the bulk of the solid is essentially equal to its value at equilibrium; thus, the bulk radiative recombination rate is no longer quadratic in the injected carrier density. Instead, under these condition, the linear (constant) radiative recombination lifetime provides a close approximation of the actual photoluminescence decay dynamics.<sup>51,57</sup> In the absence of rapid surface nonradiative recombination, the photoluminescence is relatively long-lived (compare the curve with  $k_{\text{ht}} = 10^{-17} \text{ cm}^4 \text{ s}^{-1}$  and  $N_{\text{t,s}} = 10^9 \text{ cm}^{-2}$  in Figure 3a at  $p_i/n_o = 10^{-6}$  to the corresponding curve



**TABLE 1: A Synopsis of All  $\langle\tau\rangle$  Values (eq 30) Obtained by Our Four-dimensional Parametric Simulations<sup>a</sup>**

(a) $\langle\tau\rangle$ (ns) Low Injection									
		$p_i/n_o = 10^{-6}$				$p_i/n_o = 0.5$			
		$N_{ts}\{S_p\} \text{ (cm}^{-2} \text{ {cm s}^{-1})}$				$N_{ts}\{S_p\} \text{ (cm}^{-2} \text{ {cm s}^{-1})}$			
$E - E_{fb}$ (V)	$k_{ht}$ (cm <sup>4</sup> s <sup>-1</sup> )	10 <sup>9</sup> {10 <sup>1</sup> }	10 <sup>11</sup> {10 <sup>3</sup> }	10 <sup>13</sup> {10 <sup>5</sup> }	10 <sup>15</sup> {10 <sup>7</sup> }	10 <sup>9</sup> {10 <sup>1</sup> }	10 <sup>11</sup> {10 <sup>3</sup> }	10 <sup>13</sup> {10 <sup>5</sup> }	10 <sup>15</sup> {10 <sup>7</sup> }
0	1 × 10 <sup>-17</sup>	81.6	75.2	8.6	5.2	76.3	67.2	9.2	5.3
0	2 × 10 <sup>-17</sup>	74.5	69.8	8.1	5.2	68.8	62.5	8.7	5.3
0	5 × 10 <sup>-17</sup>	60.3	57.2	7.1	5.2	54.4	51.3	7.7	5.3
0	1 × 10 <sup>-16</sup>	47.1	43.3	6.3	5.2	42.4	39.0	6.9	5.3
0.05	1 × 10 <sup>-17</sup>	52.0	47.5	4.6	4.7	50.1	44.3	5.1	4.5
0.05	2 × 10 <sup>-17</sup>	44.3	40.6	4.5	4.7	39.7	36.5	5.0	4.5
0.05	5 × 10 <sup>-17</sup>	32.1	28.4	4.4	4.7	26.8	24.6	4.7	4.6
0.05	1 × 10 <sup>-16</sup>	20.8	18.3	4.4	4.7	18.7	16.9	4.6	4.6
0.1	1 × 10 <sup>-17</sup>	25.9	24.0	4.3	4.5	21.1	19.3	3.9	4.3
0.1	2 × 10 <sup>-17</sup>	19.9	18.7	4.2	4.5	17.2	15.3	3.9	4.5
0.1	5 × 10 <sup>-17</sup>	13.1	11.9	4.3	4.5	11.4	10.6	3.9	4.3
0.1	1 × 10 <sup>-16</sup>	9.0	8.2	4.4	4.5	8.7	7.9	3.9	4.3
0.15	1 × 10 <sup>-17</sup>	11.3	10.6	4.4	4.5	9.8	8.7	3.8	4.1
0.15	2 × 10 <sup>-17</sup>	9.6	8.8	4.4	4.5	8.3	7.5	3.8	4.1
0.15	5 × 10 <sup>-17</sup>	7.2	6.6	4.4	4.5	6.7	6.0	3.8	4.1
0.15	1 × 10 <sup>-16</sup>	5.6	5.3	4.4	4.5	5.4	5.0	3.9	4.1

(b) $\langle\tau\rangle$ (ns) High Injection									
		$p_i/n_o = 2$				$p_i/n_o = 10$			
		$N_{ts}\{S_p\} \text{ (cm}^{-2} \text{ {cm s}^{-1})}$				$N_{ts}\{S_p\} \text{ (cm}^{-2} \text{ {cm s}^{-1})}$			
$E - E_{fb}$ (V)	$k_{ht}$ (cm <sup>4</sup> s <sup>-1</sup> )	10 <sup>9</sup> {10 <sup>1</sup> }	10 <sup>11</sup> {10 <sup>3</sup> }	10 <sup>13</sup> {10 <sup>5</sup> }	10 <sup>15</sup> {10 <sup>7</sup> }	10 <sup>9</sup> {10 <sup>1</sup> }	10 <sup>11</sup> {10 <sup>3</sup> }	10 <sup>13</sup> {10 <sup>5</sup> }	10 <sup>15</sup> {10 <sup>7</sup> }
0	1 × 10 <sup>-17</sup>	55.4	49.6	9.3	5.1	25.0	22.7	6.3	3.4
0	2 × 10 <sup>-17</sup>	50.3	46.5	9.0	5.1	23.1	21.3	6.2	3.6
0	5 × 10 <sup>-17</sup>	41.1	38.8	8.2	5.2	19.8	18.2	6.1	3.9
0	1 × 10 <sup>-16</sup>	32.8	30.2	7.5	5.2	15.8	14.9	5.9	4.0
0.05	1 × 10 <sup>-17</sup>	35.9	33.8	6.0	4.5	16.9	15.0	5.0	3.1
0.05	2 × 10 <sup>-17</sup>	29.7	27.8	5.8	4.5	13.7	12.4	4.9	3.3
0.05	5 × 10 <sup>-17</sup>	21.2	19.9	5.6	4.5	12.1	11.1	4.9	3.5
0.05	1 × 10 <sup>-16</sup>	15.6	14.8	5.3	4.5	10.9	10.3	4.8	3.6
0.1	1 × 10 <sup>-17</sup>	18.3	16.2	4.4	4.0	13.7	12.1	4.1	2.9
0.1	2 × 10 <sup>-17</sup>	14.0	12.6	4.3	4.0	10.5	9.4	4.1	3.1
0.1	5 × 10 <sup>-17</sup>	10.7	9.8	4.2	4.0	8.1	7.3	4.2	3.2
0.1	1 × 10 <sup>-16</sup>	8.8	7.8	4.1	4.0	6.7	6.0	4.0	3.4
0.15	1 × 10 <sup>-17</sup>	9.5	8.2	3.5	3.6	8.2	7.3	3.2	2.7
0.15	2 × 10 <sup>-17</sup>	7.5	6.8	3.5	3.6	6.6	5.8	3.5	2.6
0.15	5 × 10 <sup>-17</sup>	6.3	5.8	3.4	3.4	5.4	4.9	3.5	3.0
0.15	1 × 10 <sup>-16</sup>	5.2	4.9	3.4	3.4	3.7	3.4	3.5	3.2

<sup>a</sup> The influence of band bending on the photoluminescence decays for various combinations of charge-transfer rate constants,  $k_{ht}$ , and surface states densities,  $N_{ts}$  (or surface recombination velocities,  $S_p$ ) is tabulated for injection levels ranging from (a) low injection ( $p_i/n_o$  of 10<sup>-6</sup> and 0.5) to (b) high injection ( $p_i/n_o$  of 2.0 and 10).

in Figure 2a at  $p_i/n_o = 10$ ). In fact, the long-lifetime photoluminescence decay asymptote under these conditions is dictated only by nonradiative recombination in the bulk of the semiconductor, which has a 100 ns lifetime at the chosen bulk trap concentration.

As was the case for high-level injection, the short-time asymptote is reached when the rate of surface recombination and/or interfacial charge transfer is equal to, or greater than, the rate at which carriers can reach the surface by diffusion. Increasing  $N_{ts}$  thus decreases the range over which  $k_{ht}$  can be measured. An extreme example of this situation is observed in Figure 3d for  $N_{ts} = 10^{15}$  cm<sup>-2</sup> ( $S_p = 10^7$  cm s<sup>-1</sup>), where nonradiative surface recombination is so rapid that the value of  $k_{ht}$  has essentially no influence on the photoluminescence decay dynamics. For similar reasons, regardless of how small  $N_{ts}$  was made, the decays were insensitive to increases in  $k_{ht}$  above  $k_{ht} = 5 \times 10^{-15}$  cm<sup>4</sup> s<sup>-1</sup> under these conditions.

**C. Effect of Bias Potential.** The other important process that can quench the photoluminescence is diffusion of charge carriers to the space-charge layer. Once in the space-charge layer, carriers are promptly separated by the electric field in this region of the semiconductor. Almost no radiative recombination can occur in the depletion region near the solid/liquid contact because very few majority carriers are present in this

region.<sup>10,33,34,40,44,65,79,80,84</sup> Thus, the photoluminescence signal will rapidly decay if minority carriers diffuse into the space-charge region even if these carriers do not recombine but instead merely accumulate at or near the solid/liquid interface.

**1. Bias Dependence in High-Level Injection.** Under high-level injection conditions ( $p_i/n_o = 10$ ), the photoluminescence decay dynamics exhibited essentially no bias dependence for  $N_{ts} \geq 10^{12}$  cm<sup>-2</sup> ( $S_p \geq 10^4$  cm s<sup>-1</sup>). Only for  $N_{ts} < 10^{11}$  cm<sup>-2</sup> did the photoluminescence decay curves vary, changing from a relatively fast 25 ns lifetime to a 4 ns lifetime when  $k_{ct} \leq 10^{-17}$  cm<sup>4</sup> s<sup>-1</sup>, as  $E$  was changed from flat band to 0.15 V positive of flat band. The reasons for this behavior involve flattening of the bands and loss of potential control due to the high level of carrier injection produced by the intense optical injection pulse. For example, at  $E = 0.15$  V and  $p_i/n_o = 10$ , with  $N_{ts} = 10^{11}$  cm<sup>-2</sup> and  $k_{ht} = 10^{-16}$  cm<sup>4</sup> s<sup>-1</sup>, the band bending in the solid immediately after the injection pulse was 0.03 V; for  $E = 0.3$  V and identical values of the other parameters, the band bending in the solid immediately after the injection pulse was only 0.06 V. For high-level injection, the photoluminescence decays of Figure 2 are thus representative, with only small modifications, not only of the decays at flat band but at other potentials in reverse bias as well.

**2. Bias Dependence in Low-Level Injection.** In contrast,

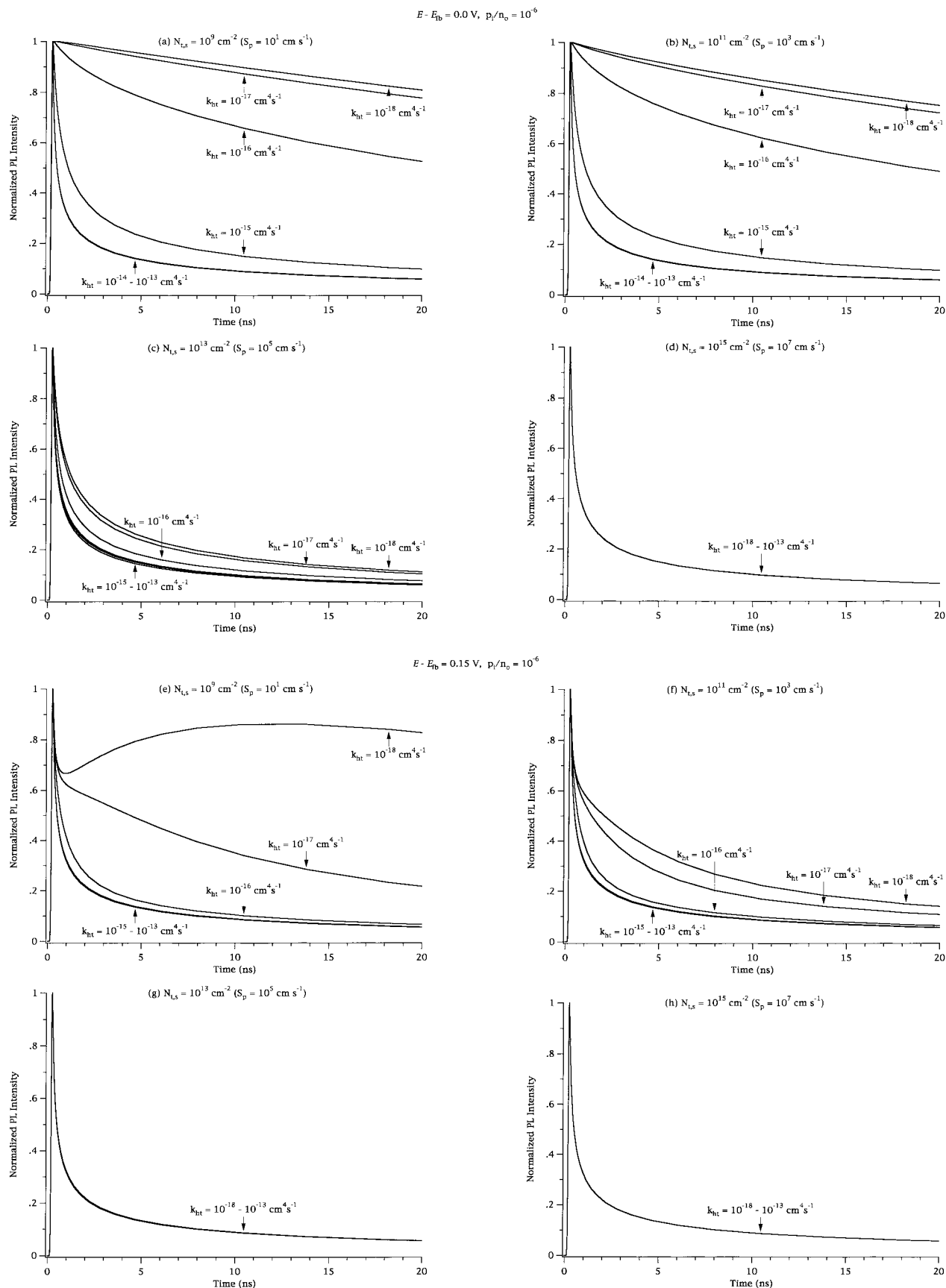


**Figure 3.** Simulated photoluminescence transients at the low injection level ( $p_i/n_o$ ) of  $10^{-6}$ . Panels a, b, c, and d illustrate the influence of  $k_{ht}$  on photoluminescence decays under flat-band potential conditions for  $N_{t,s}$  ( $S_p$ ) values of (a)  $10^9$  ( $10$ ), (b)  $10^{11}$  ( $10^3$ ), (c)  $10^{13}$  ( $10^5$ ), and (d)  $10^{15}$  ( $10^7$ )  $\text{cm}^{-2}$  ( $\text{cm s}^{-1}$ ), respectively. For comparisons at a higher band bending, panels e, f, g, and h illustrate the influence of  $k_{ht}$  on the photoluminescence decays at a reverse bias of 0.15 V vs the flat-band potential for  $N_{t,s}$  ( $S_p$ ) values of (e)  $10^9$  ( $10$ ), (f)  $10^{11}$  ( $10^3$ ), (g)  $10^{13}$  ( $10^5$ ), and (h)  $10^{15}$  ( $10^7$ )  $\text{cm}^{-2}$  ( $\text{cm s}^{-1}$ ), respectively.

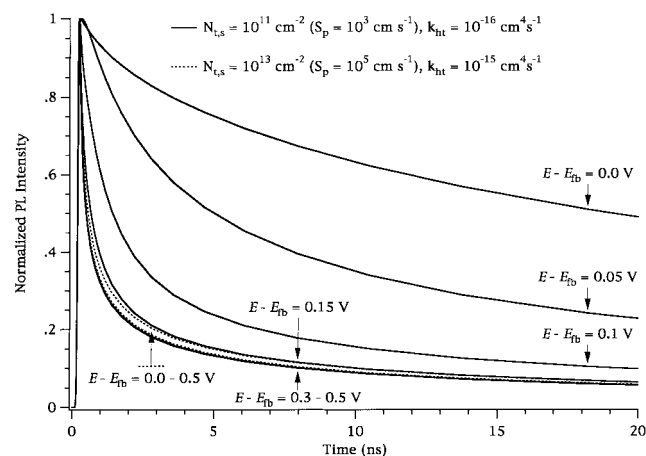


**Figure 4.** Simulated photoluminescence transients at the low injection level ( $p_i/n_o$ ) of  $10^{-6}$ . The influence of band bending on the photoluminescence decays, for which  $N_{ts} = 10^{11} \text{ cm}^{-2}$  ( $S_p = 10^3 \text{ cm s}^{-1}$ ) and  $k_{ht} = 10^{-16} \text{ cm}^4 \text{ s}^{-1}$  (solid lines) or  $N_{ts} = 10^{13} \text{ cm}^{-2}$  ( $S_p = 10^5 \text{ cm s}^{-1}$ ) and  $k_{ht} = 10^{-15} \text{ cm}^4 \text{ s}^{-1}$  (dotted lines) is illustrated. At this low injection level, no distinctions between photoluminescence transients in which  $N_{ts} = 10^{11} \text{ cm}^{-2}$  ( $S_p = 10^3 \text{ cm s}^{-1}$ ) and  $k_{ht} = 10^{-16} \text{ cm}^4 \text{ s}^{-1}$  (solid lines) can be made once the degree of band bending surpassed 0.15 V. The simulated photoluminescence decays for  $N_{ts} = 10^{13} \text{ cm}^{-2}$  ( $S_p = 10^5 \text{ cm s}^{-1}$ ) and  $k_{ht} = 10^{-15} \text{ cm}^4 \text{ s}^{-1}$  (dotted lines) are indistinguishable from each other under all reverse-bias conditions and are likewise indistinguishable for photoluminescence decays for which  $N_{ts} = 10^{11} \text{ cm}^{-2}$  ( $S_p = 10^3 \text{ cm s}^{-1}$ ),  $k_{ht} = 10^{-16} \text{ cm}^4 \text{ s}^{-1}$ , and  $E \geq 0.15 \text{ V}$  (solid lines).

under low- or intermediate-level injection conditions, increasing reverse bias induces more rapid charge separation and thus more rapid photoluminescence decay. This behavior can be seen in a comparison of the low-level injection photoluminescence decay dynamics obtained at  $E = 0$ , Figures 3a–d, to those simulated at a relatively small reverse bias of  $E = 0.15 \text{ V}$ , as displayed in Figures 3e–h.

The decays for given values of  $N_{ts}$  and  $k_{ht}$  are almost all more rapid for  $E = 0.15 \text{ V}$  than for  $E = 0 \text{ V}$  (compare Figures 3a–d to 3e–h, except for  $N_{ts} = 10^9 \text{ cm}^{-2}$ ,  $k_{ht} < 10^{-17} \text{ cm}^4 \text{ s}^{-1}$ ) until the short-time asymptotic behavior is reached at each bias potential. After this limit is reached, the photoluminescence decays are almost completely insensitive to the value of  $k_{ht}$ . Even for small values of  $N_{ts}$ , the range over which the photoluminescence decays are sensitive to  $k_{ht}$  becomes significantly smaller as the electrode is biased into depletion (cf. Figures 3a–c to Figures 3e–g).

Photoluminescence decay curves obtained with band bending beyond  $E = 0.15 \text{ V}$  yield even less information on the values of  $k_{ht}$  and  $S_p$ . As can be seen in Figure 4, essentially no dependence on  $k_{ht}$  or  $N_{ts}$  is observed for  $E > +0.15 \text{ V}$  for  $p_i/n_o < 0.1$ .

This behavior can be readily understood through consideration of the rates of drift and diffusion relative to the rate(s) of surface recombination and/or charge-transfer at the semiconductor/liquid contact. In contrast to the situation at the flat-band potential or to that observed under high-level injection, in the presence of an electric field it is not necessary that carriers recombine nonradiatively as rapidly as they reach the surface in order to obtain the short-time asymptote of the photoluminescence decay. Even if surface recombination and interfacial charge transfer are relatively slow, the short-time asymptote will be observed provided that carriers can diffuse into the space-charge region.<sup>33,34,41–44</sup>

As displayed in Figure 4, for  $E \geq +0.15$ , different biases produce marginally different photoluminescence decay dynamics because the moderately increased space-charge width at higher reverse biases separates charge carriers slightly more effectively. However, because the majority carrier concentration is not perturbed significantly by the illumination, the photoluminescence decay dynamics under low-level injection for  $E > +0.15 \text{ V}$  are almost completely controlled by the value of  $E$  and do not yield any information on  $N_{ts}$  or  $k_{ht}$ . This loss in ability to determine  $N_{ts}$  or  $k_{ht}$  under low injection when  $E > 0.15 \text{ V}$  is clearly illustrated in Figure 4, where no distinctions can be made between photoluminescence decays with  $N_{ts} = 10^{11} \text{ cm}^{-2}$ ,  $k_{ht} = 10^{-16} \text{ cm}^4 \text{ s}^{-1}$ , and  $E \geq 0.15 \text{ V}$  (solid lines) and photoluminescence decays with  $N_{ts} = 10^{13} \text{ cm}^{-2}$ ,  $k_{ht} < 10^{-15} \text{ cm}^4 \text{ s}^{-1}$  and  $E \geq 0.0 \text{ V}$  (dotted lines).

The simulations also illustrate the difficulty in distinguishing between changes in  $N_{ts}$  and changes in  $k_{ht}$  from data for  $E > 0.15 \text{ V}$ . For  $E > 0.10 \text{ V}$ , essentially any  $k_{ht}$  value from  $10^{-18}$  to  $10^{-13} \text{ cm}^4 \text{ s}^{-1}$  produced the same photoluminescence decay. Similarly, for  $E > 0.10 \text{ V}$ , the photoluminescence decays were essentially insensitive to the value of  $N_{ts}$ . This behavior underscores the importance of separating surface recombination from charge transfer in the boundary conditions of the simulation; otherwise artificially large  $S_p$  values will be required in order to fit a given photoluminescence decay obtained under these experimental conditions. In accordance with Table 1, a fit parametrized by  $N_{ts} = 10^{15} \text{ cm}^{-2}$  ( $S_p = 10^7 \text{ cm s}^{-1}$ ) and  $k_{ht} = 10^{-17} \text{ cm}^4 \text{ s}^{-1}$  at  $E = 0 \text{ V}$  would readily fit virtually all of the photoluminescence decays simulated at  $N_{ts} > 10^{12} \text{ cm}^{-2}$  and  $E \geq 0.05 \text{ V}$ , especially under high-level injection.

It is interesting to note that with very low surface recombination velocities ( $S = 10^1 \text{ cm s}^{-1}$ ) and very low charge-transfer rate constants ( $k_{ht} = 10^{-18} \text{ cm}^4 \text{ s}^{-1}$ ), at  $E = 0.15 \text{ V}$ , the photoluminescence signal did not exhibit a monotonic decay with time (Figure 3e). Instead, the signal exhibited an increase after the initial decline in intensity and then monotonically decayed to zero. This phenomenon is predicted to occur because of the subtle interplay between the various diffusion, drift, and recombination processes simultaneously occurring under these specific conditions. Initially a significant amount of the luminescence signal is produced from radiative decay processes occurring at the edge of the space-charge region of the semiconductor. The photoluminescence signal then declines in intensity as the carriers that contribute to this luminescence signal either recombine or are separated in the space-charge layer. The field-induced charge separation, however, produces an increased minority carrier concentration at the surface of the solid. Thus, for a brief time period, the radiative recombination rate at the surface is dominant because the concentration of minority carriers at the surface is increased. After some additional period of time, the majority and minority carrier concentrations then decrease again so that the photoluminescence signal exhibits a monotonic decay toward zero signal amplitude. This interesting interplay between the various generation, transport, and recombination mechanisms is only observed over a very small region of parameter space, as displayed in Figure 3.

**3. Bias Dependence in Intermediate-Level Injection.** Simulations were also performed for an intermediate-injection level of  $p_i/n_o = 0.5$ . This value corresponds to the injection levels used in the past (from focused laser beams) to produce what were believed to be high-level injection conditions.<sup>26,80</sup> As depicted in Figure 5a, the simulations showed that for  $E > +0.05 \text{ V}$ , the photoluminescence decays for  $p_i/n_o = 0.5$  were

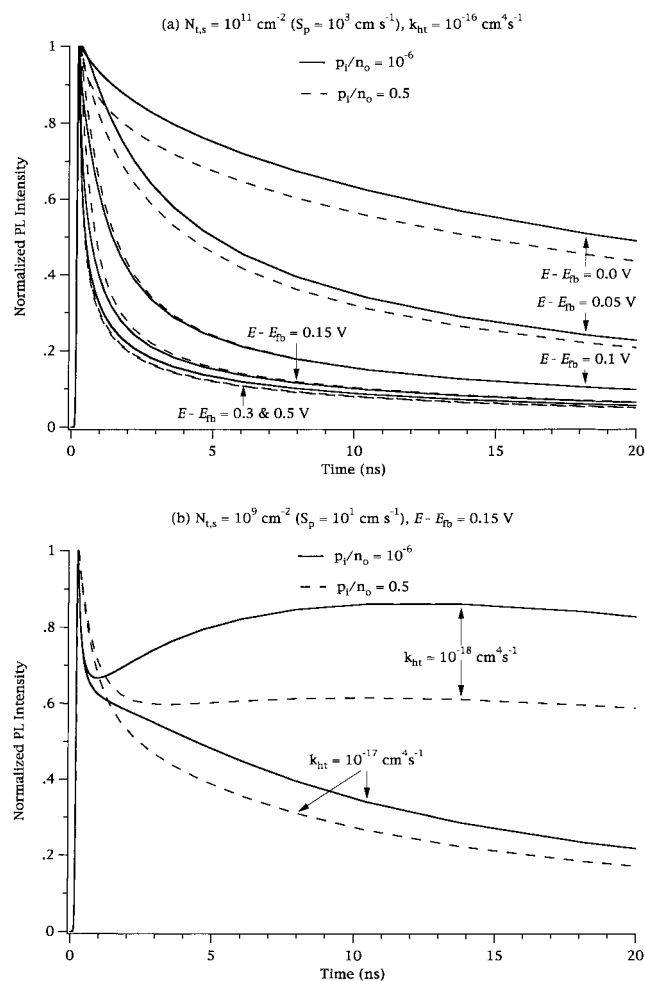


**Figure 5.** Simulated photoluminescence transients. (a) The influence of band bending on photoluminescence decays, for which  $N_{ts} = 10^{11} \text{ cm}^{-2}$  ( $S_p = 10^3 \text{ cm s}^{-1}$ ) and  $k_{ht} = 10^{-16} \text{ cm}^4 \text{ s}^{-1}$  for injection levels ( $p_i/n_o$ ) of  $10^{-6}$  (solid lines) and 0.5 (dashed lines) is illustrated. The two injection cases produce identical decays for all reverse biases greater than 0.05 V vs the flat-band potential. (b) Simulations revealing that for biases greater than 0.05 V an extremely narrow boundary exists where  $N_{ts} \leq 10^9 \text{ cm}^{-2}$  ( $S_p \leq 10^1 \text{ cm s}^{-1}$ ) and  $k_{ht} \leq 10^{-17} \text{ cm}^4 \text{ s}^{-1}$  in which variances between photoluminescence decays with injection levels ( $p_i/n_o$ ) of  $10^{-6}$  and 0.5 occur.

essentially identical to those obtained in the low-level injection cases discussed above. Only under flat-band potential conditions, or for  $E = +0.05 \text{ V}$ , and at the lowest values of  $N_{ts}$  and  $k_{ht}$  were changes in the photoluminescence decay dynamics observed due to this increased level of injection. Figure 5b compares the simulations for these injection level conditions to those obtained for low-level injection conditions ( $p_i/n_o < 10^{-1}$ ) in regions where significant differences were observed in the photoluminescence decay dynamics between the two injection levels, that is, for regions where  $S = 10 \text{ cm s}^{-1}$  and  $E = 0.15 \text{ V}$ .

Analysis of the simulation's carrier concentration profiles immediately after illumination revealed the reasons for this behavior. As an illustrative example, at a bias of  $E = +0.50 \text{ V}$ , the equilibrium majority carrier concentration at the electrode surface is only  $10^8 \text{ cm}^{-3}$ , as compared to the value in the bulk of  $n_o = 5 \times 10^{15} \text{ cm}^{-3}$ . The injection pulse produces far more majority carriers at the surface than are present in the dark, so based on the total carrier concentrations injected into the semiconductor during the laser pulse, the bands would be expected to be significantly flattened immediately following the laser pulse. However, simulations revealed that the carrier

concentration profile in the solid was almost the same immediately after the laser pulse as it was in the dark. For example, at  $E = 0.50 \text{ V}$ ,  $N_{ts} = 10^{11} \text{ cm}^{-2}$ , and  $k_{ht} = 10^{-16} \text{ cm}^4 \text{ s}^{-1}$ , the band bending immediately after the pulse for an injection level of  $p_i/n_o = 0.5$  was still 0.47 V. Thus, even injection levels of  $p_i/n_o = 0.5$  can be viewed as low-level injection conditions under the simulated experimental conditions.

This lack of band flattening occurs because charge carrier separation in the depletion region proceeds so rapidly that carriers are separated during, and promptly after, the laser pulse. The charge separation process restores the carrier concentration profiles to their equilibrium values, and the luminescence decay is then dominated by diffusion of carriers from the bulk of the solid into the space-charge region, where they are separated, thus quenching the luminescence. As for all other low-level injection conditions, only  $E$ , as opposed to  $k_{ht}$  or  $N_{ts}$ , determines the form of the photoluminescence decay dynamics for  $p_i/n_o = 0.5$  and  $E > +0.10 \text{ V}$ .

For biases very close to the flat-band potential, some differences were observed in the photoluminescence decay dynamics between injection levels of  $p_i/n_o = 0.5$  and  $p_i/n_o < 10^{-1}$ . These differences are readily explained because without a significant electric field to separate the injected charge carriers, the carrier concentrations in the solid are initially significantly perturbed by the laser pulse. In this regime diffusional processes, along with some drift-induced charge separation, dominate the shape of the photoluminescence decay dynamics. Because the initial photoluminescence signal is first-order in both the electron and hole concentrations in the semiconductor, the photoluminescence signal therefore decays somewhat more rapidly near  $E = 0 \text{ V}$  for  $p_i/n_o = 0.5$  than it does for  $p_i/n_o < 0.1$  (Figure 5a). For injection levels of either  $p_i/n_o = 10$ ,  $p_i/n_o = 0.5$ , or  $p_i/n_o = 10^{-6}$  and for  $E > 0.15 \text{ V}$ , no circumstances existed whereby it was possible to identify reverse bias conditions where a dependence of the  $N_{ts}$  and  $k_{ht}$  values on the value of  $E$  could be readily determined experimentally.

**D. Influence of the Spatial Profile of the Laser Excitation Pulse on the Photoluminescence Decays.** The two-dimensional simulation code of ToSCA also provided insight into the effect of spatially inhomogeneous illumination on the simulated photoluminescence decays. This effect is expected to become important when the laser beam dimensions are comparable to the minority carrier diffusion length of the sample.<sup>85</sup> To investigate this effect, the photoluminescence decay dynamics were simulated for various spatial profiles of the laser excitation source. During this process, the injection level, calculated from the number of photons absorbed in a volume element of a depth equal to  $\alpha^{-1}$ , of a width equal to the  $1/e^2$  width of the laser beam's spatial profile, and of a height equal to  $32 \mu\text{m}$ , was kept constant, as were all other intensive parameters and kinetic parameters of the simulation. Since in these simulations the latter, third, dimension was considered uniform and quasi-infinite, the actual excitation profile was thus a strip which is infinitely long, of width equal to the  $1/e^2$  width of the laser beam's spatial profile, and of depth equal to  $\alpha^{-1}$ .

Figure 6 depicts the ToSCA simulations obtained for these various illumination areas. Figure 6a illustrates the photoluminescence decays with  $32 \mu\text{m}$  and  $6 \mu\text{m}$  laser beam widths for  $N_{ts} = 10^{11} \text{ cm}^{-2}$  and  $k_{ht} = 10^{-16} \text{ cm}^4 \text{ s}^{-1}$  at the flat-band potential. Figure 6b illustrates the photoluminescence decays with boundary conditions similar to those in Figure 6a except with the bias set to  $E = 0.15 \text{ V}$  positive from the flat-band potential. The simulations were run with injection levels ( $p_i/n_o$ ) of 0.5 (which is representative of all  $p_i/n_o \leq 10^{-1}$ ) and 10.



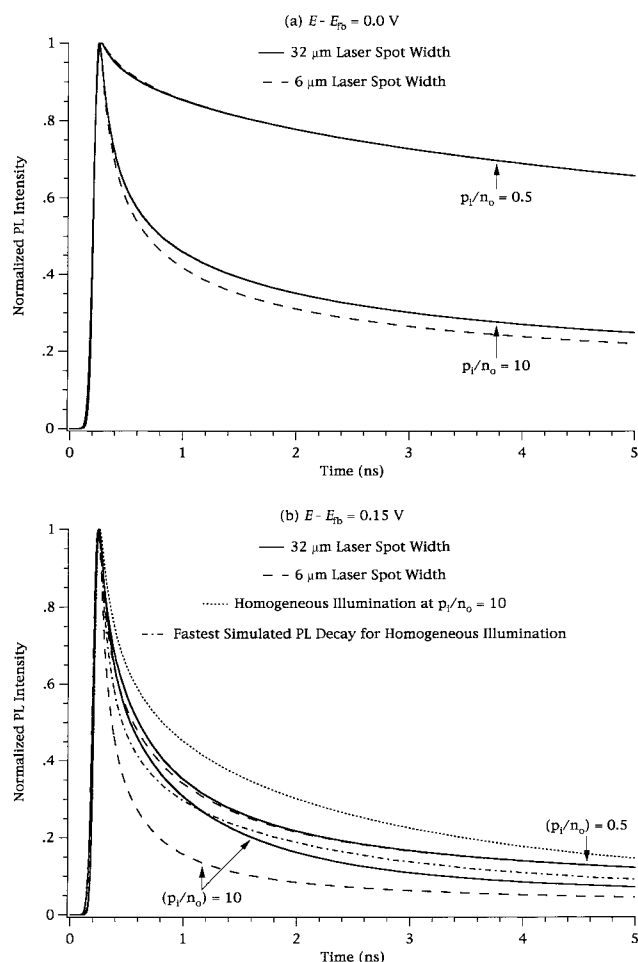


**Figure 6.** Influence of varying the laser spot width from 32  $\mu\text{m}$  to 6  $\mu\text{m}$  on the photoluminescence decays for which  $N_{\text{ts}} = 10^{11} \text{ cm}^{-2}$  ( $S_p = 10^3 \text{ cm s}^{-1}$ ) and  $k_{\text{ht}} = 10^{-16} \text{ cm}^4 \text{ s}^{-1}$  is illustrated for injection levels ( $p_i/n_o$ ) of 0.5 and 10 at reverse biases of (a)  $E = 0.0 \text{ V}$  from flat-band potential and (b)  $E = 0.15 \text{ V}$  from flat-band potential. For reference, panel b shows the photoluminescence decay obtained at homogeneous illumination (dotted line) for  $N_{\text{ts}} = 10^{11} \text{ cm}^{-2}$  ( $S_p = 10^3 \text{ cm s}^{-1}$ ),  $k_{\text{ht}} = 10^{-16} \text{ cm}^4 \text{ s}^{-1}$ , and  $E = 0.15 \text{ V}$  and the fastest simulated photoluminescence decay obtained for homogeneous illumination (dotted-dashed line).

For reference, the photoluminescence decay profile simulated with homogeneous illumination at  $E = 0.15 \text{ V}$  for  $N_{\text{ts}} = 10^{11} \text{ cm}^{-2}$ ,  $k_{\text{ht}} = 10^{-16} \text{ cm}^4 \text{ s}^{-1}$ , and an injection level of 10 is illustrated by the dotted line in Figure 6b. Additionally, the simulated photoluminescence decay represented by the alternately dashed and dotted line in Figure 6b illustrates the most rapidly decaying photoluminescence data that could be simulated for homogeneous illumination (any decay profile with  $N_{\text{ts}} > 10^{15} \text{ cm}^{-2}$ ,  $k_{\text{ht}} > 10^{-15} \text{ cm}^4 \text{ s}^{-1}$ ,  $p_i/n_o = 10$ , and  $E > 0.15 \text{ V}$ ).

As can be seen from the upper pair of curves in Figure 6a, the only case for which varying the spot size had no influence on the photoluminescence decay profile was at the flat-band potential under moderate injection ( $p_i/n_o = 0.5$ ). With the boundary conditions employed here, the 32  $\mu\text{m}$ , the 6  $\mu\text{m}$ , and the homogeneous illumination (not shown) laser profiles produced the same decay profiles. However, significant variations in the photoluminescence decay dynamics were observed as the illumination spot size was varied at the flat-band potential under high-level injection. In addition, significant variations in the photoluminescence decay dynamics were observed as a function of spot size for all the simulations at  $E = 0.15 \text{ V}$ , as shown in Figure 6b.

Two principal phenomena contribute to the more rapid decays observed for smaller laser spot sizes. First, second-order radiative recombination is much more rapid for small beam diameters. Second, the photoexcited carriers in the smaller beam area are much closer to, that is, within a few diffusion lengths from, regions of large band bending in unilluminated regions on the electrode surface. Thus, lateral diffusion and lateral drift currents can quench the luminescence of carriers in the photoexcited region of the solid in the same way that they quench the luminescence in a direction normal to the semiconductor/liquid interface. The physical situation present under these circumstances cannot be faithfully captured using a one-dimensional simulation.

The decays observed in the two-dimensional simulation at small laser spot sizes are significantly more rapid than those obtained in the corresponding one-dimensional simulation with homogeneous illumination at the same injection level. In fact, use of a one-dimensional simulation routine suggested that a best-fit value to the 32  $\mu\text{m}$ ,  $E = 0.15 \text{ V}$ , and  $p_i/n_o = 10$  data of Figure 6b was obtained with  $N_{\text{ts}} > 10^{13} \text{ cm}^{-2}$  ( $S_p > 10^5 \text{ cm s}^{-1}$ ) and  $k_{\text{ht}} > 10^{-15} \text{ cm}^4 \text{ s}^{-1}$ , but the decay dynamics actually corresponded to a two-dimensional scenario having  $N_{\text{ts}} = 10^{11} \text{ cm}^{-2}$  ( $S_p = 10^3 \text{ cm s}^{-1}$ ) and  $k_{\text{ht}} = 10^{-16} \text{ cm}^4 \text{ s}^{-1}$ . With respect to the fastest photoluminescence decay presented in Figure 6b, observed under high injection, at  $E = 0.15 \text{ V}$ , using a 6  $\mu\text{m}$  laser spot size and with  $N_{\text{ts}} = 10^{11} \text{ cm}^{-2}$  ( $S_p = 10^3 \text{ cm s}^{-1}$ ) and  $k_{\text{ht}} = 10^{-16} \text{ cm}^4 \text{ s}^{-1}$ , ToSCA's trap model was unable to simulate this decay profile using any combination of parameters under homogeneous illumination.

Experimentally observed photoluminescence decay transients would, in fact, be even more rapid than those simulated, because the two-dimensional simulation does not account for any luminescence quenching in the other (third, unsimulated) dimension parallel to the solid/liquid interface. At present, we are incorporating such three-dimensional features into ToSCA; however, for the purposes of this work it suffices to state that severe overestimates of  $k_{\text{ht}}$  result when one-dimensional simulation routines are used to model experimental data collected using inhomogeneously illuminated samples and small laser spot sizes. These simulations are of importance because in many experiments the illumination intensity is increased by focusing a laser beam to attain intermediate injection levels using routinely available laser beam powers.<sup>30,35</sup> Without a complete three-dimensional simulation routine, the most reliable comparison between simulations and experimental data will be obtained through use of uniform, homogeneous illumination of the sample and reference to the simulations depicted in Figures 2–5.

**E. Effects of Using Steady-State vs Dynamic Trapping Boundary Conditions in the Analysis of Photoluminescence Decay Data.** It is useful to compare the simulation results obtained using the steady-state SRH model for surface recombination to the results obtained from the trap model utilized in this work. To perform this comparison, the low-level injection surface recombination velocity was set to  $10^3 \text{ cm s}^{-1}$ , which would correspond to the situation for  $N_{\text{ts}} = 10^{11} \text{ cm}^{-2}$  with  $k_{\text{n,s}} = k_{\text{p,s}} = 10^{-8} \text{ cm}^3 \text{ s}^{-1}$  in the trap model at low-level injection. To illustrate the distinction between the two models, the influence of changing  $k_{\text{ht}}$  at fixed  $S_p$  was investigated at two different band-bending values. Figure 7 depicts the results of such a comparison. The injection level (of a homogeneous beam illuminated over the entire sample) was fixed at  $p_i/n_o = 0.5$ . To assist in these comparisons, corresponding photolumines-

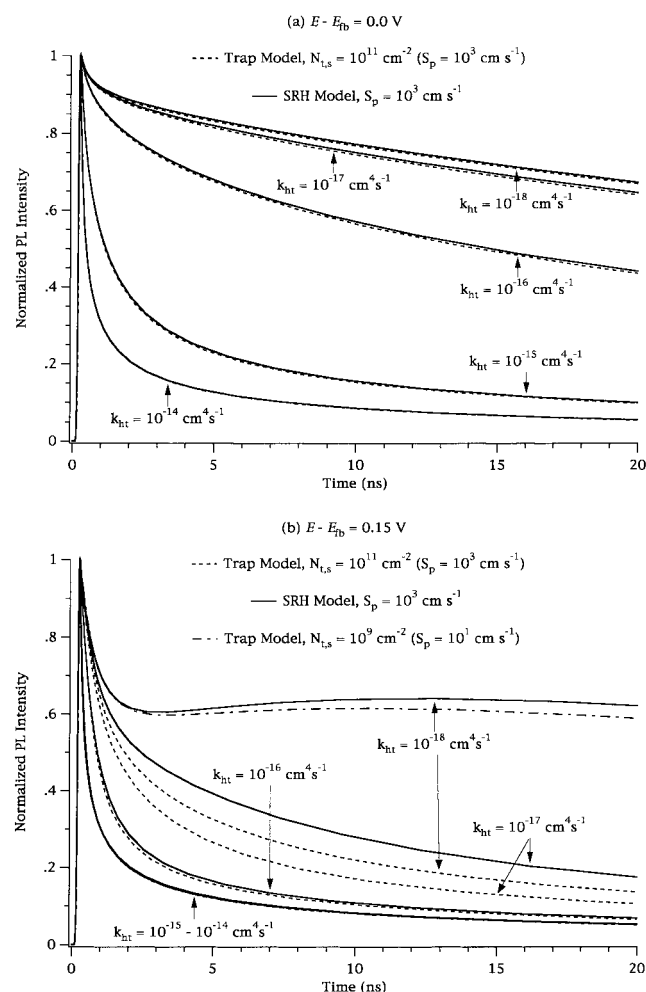


**Figure 7.** Simulated photoluminescence transients for which  $S_p = 10^3$  cm s<sup>-1</sup> at an injection level ( $p_i/n_0$ ) of 0.5, for various  $k_{ht}$  values. These panels illustrate how dissimilar the photoluminescence decays for the SRH (solid lines) and trap model (dashed lines) become as the reverse bias is varied from (a)  $E = 0.0$  V from flat band to (b)  $E = 0.15$  V from flat band and thus illustrates the degree of overestimation in determining  $S_p$  or  $k_{ht}$  produced by use of the SRH model rather than the trap model. The  $S_p$  in the SRH model was equal to  $10^3$  cm s<sup>-1</sup> for all the decays shown. The dash-dotted line corresponds to a trap model photoluminescence decay in which  $N_{ts} = 10^9$  cm<sup>-2</sup> ( $S_p = 10^1$  cm s<sup>-1</sup>) and  $k_{ht} = 10^{-18}$  cm<sup>4</sup> s<sup>-1</sup>.

cence decays obtained from ToSCA have been overlaid as dotted lines in Figure 7.

A comparison between the SRH model (solid lines) and the trap model (dotted lines) at the flat-band potential, Figure 7a, reveals that the two models are comparable under these conditions. The SRH model overestimates the photoluminescence decay lifetimes by <3% in these instances. Figure 7b, however, shows the significant differences observed between the models for the simulations run with  $E = 0.15$  V and  $k_{ht} < 10^{-16}$  cm<sup>4</sup> s<sup>-1</sup>. For these simulations, the SRH model produced photoluminescence decays similar to those obtained with the trap model, but in some cases, the SRH model required  $S_p$  values 2 orders of magnitude larger than those used in the trap model in order to simulate the decays. Such a scenario can be seen in the upper pair of curves in Figure 7b, which correspond to a SRH-model photoluminescence decay (solid line) with  $S_p = 10^3$  cm s<sup>-1</sup> and  $k_{ht} = 10^{-18}$  cm<sup>4</sup> s<sup>-1</sup> and to a trap-model simulation (dash-dotted line) with  $N_{ts} = 10^9$  cm<sup>-2</sup> ( $S_p = 10^1$  cm s<sup>-1</sup>) and  $k_{ht} = 10^{-18}$  cm<sup>4</sup> s<sup>-1</sup>. This discrepancy occurs because in the steady-state model surface recombination is minimal at reverse

bias because there are relatively few majority carriers available to participate in the surface recombination events. In reality, however, as long as the number of surface traps occupied by majority carriers exceeds the number of injected minority carriers, a minority carrier trapping process can quench the luminescence without involving any majority carrier transfer steps. For the boundary conditions represented by the simulated photoluminescence decays of Figure 7, the total number of surface traps exceeds the number of injected minority carriers by a factor of 2.3. This physical situation is not captured by the boundary conditions of eqs 10 and 12 but is accurately represented by those of eqs 18–23. The use of the steady-state SRH model of eq 12 thus always leads to overestimates of the surface recombination velocity of the solid/liquid contact, because in the SRH model the value of  $S_p$  used to fit the experimental data must be very large in order to effectively capture minority carriers at large band-bending values. This effect, combined with the shortcomings of a one-dimensional treatment of small illumination areas described above, must be carefully considered in any analysis of existing experimental data intended to determine the values of key interfacial kinetic properties of a semiconductor/liquid interface.

#### IV. Conclusions

For a semiconductor that is illuminated with short laser pulses, quasi-equilibrium will not be established and the steady-state assumptions employed in the derivation of eqs 13–17, whereby the surface recombination dynamics can be modeled by an effective surface recombination velocity, are no longer valid. Since under these conditions the luminescence is quenched by carriers entering the space-charge (dead) layer,  $S_{eff}$  is not a measure for the actual surface processes but, instead, reflects the rate for diffusion of carriers leaving the bulk and entering the space-charge region. Thus, models based on the steady-state equations intertwine diffusional quenching and surface recombination. The net result of this convolution is a series of parametrized fits that yield values for the surface recombination velocity that are of a magnitude more commensurate with diffusional velocities than with the actual surface recombination velocities. The simulations presented in this study treat all processes separately and produce photoluminescence decays that are representative of the actual carrier decay dynamics of the solid/liquid contact. These simulated photoluminescence decays clearly separate the role of diffusion and surface recombination and yield the result that in the diffusional limit decays with varying surface recombination velocities do indeed have the same decay lifetimes.

The simulations that have been performed herein treat the majority and minority carrier charge-transfer dynamics separately through use of a dynamic trapping kinetic model. The simulations account for transport in two dimensions, one parallel and one normal to the semiconductor/liquid interface, and also incorporate a field-dependent electron mobility in the bulk of the semiconductor. The simulations reveal that for a limited regime bordered by  $N_{ts} \leq 10^{12}$  cm<sup>-2</sup>,  $k_{ht} < 10^{-15}$  cm<sup>4</sup> s<sup>-1</sup>, and  $E < 0.15$  V,  $k_{ht}$  and surface recombination velocity values can be determined independently from experimental photoluminescence decay data. In this regime, the simulations provide a quantitative framework for analysis of the experimental photoluminescence decay data at semiconductor/liquid contacts. For  $E \geq 0.15$  V, the photoluminescence decays were relatively insensitive to  $k_{ht}$  and were dominated by diffusion of minority carriers from the bulk to the space-charge layer, where field-induced charge separation prevented further radiative recombination. Thus, this study suggests that no conclusions con-

## Glossary

parameter(s)	description	value(s) used in simulations or definition(s) of parameters
$\alpha$	Optical absorption coefficient for InP	$5.9 \times 10^4 \text{ cm}^{-1}$ (@ 670 nm)
$A_1$ & $A_2$	Pre-exponential of the biexponential fit of a photoluminescence decay	eq 29
$c_{\text{red}} (c_{\text{ox}})$	Dissolved concentration of electron donors (acceptors) in the solution	$c_{\text{red}} = c_{\text{ox}} = 0.10 \text{ M}$
$C_n (C_p)$	Auger recombination coefficient for electrons (holes)	$C_n = C_p = 10^{-31} \text{ cm}^6 \text{ s}^{-1}$
$d$	InP sample thickness	$200 \mu\text{m}$
$\epsilon$	Dielectric constant of the InP semiconductor	$12.35\epsilon_0$
$\epsilon_0$	Dielectric constant in vacuum	$8.85 \times 10^{-14} \text{ F cm}^{-1}$
$\epsilon_{\text{H}}$	Dielectric constant of the Helmholtz layer	$6 \epsilon_0$
$\mathcal{E}$	Electric field strength in the semiconductor	eq 28
$\mathcal{E}_{\text{crit}}$	Critical electric field strength for InP	$12 \text{ keV}$
$E$	Voltage drop across the semiconductor	$0.0 \text{ V} \leq E \leq 0.5 \text{ V}$ positive of $E_{\text{fb}}$
$E_{\text{fb}}$	Flat-band potential of the semiconductor–liquid system	$(1/q)\mathbf{E}_{\text{f}} - V_{\text{bi}}$
$E_{\text{f}}$	Fermi level energy	$\mathbf{E}_{\text{f}} \equiv 0.0 \text{ eV}$
$E_{\text{F,n}} (E_{\text{F,p}})$	Quasi–Fermi levels for electrons (holes)	(in units of eV)
$E_{\text{g}}$	InP band-gap energy	$1.35 \text{ eV}$
$E_{\text{i}}$	InP intrinsic energy level	ref 56
$E_{\text{redox}}^{\circ}$	Formal electrochemical potential of the redox couple in solution	$0.8 \text{ eV}$ relative to $E_{\text{c}}$
$E_{\text{t}}$	energy of a trap state	$0.0 \text{ eV}$ relative to $E_{\text{i}}$
$E_{\text{v}} (E_{\text{c}})$	Energy of the valence (conduction) band edge, function of position	(in units of eV)
$f_{\text{t}}$	Fraction of traps occupied by electrons	eq 10 (steady-state models) eq 23 (trap model)
$G$	Beer–Lambert optical generation function	eq 19
$I_{\text{PL}}(t)$	Photoluminescence intensity as a function of time	eq 29
$j_{\text{c}} (j_{\text{v}})$	Charge-transfer current to and from the conduction (valence) band	eqs 24–25
$j_{\text{n}} (j_{\text{p}})$	Electron (hole) current density at the semiconductor/liquid interface	eqs 5–6
$J_{\text{n}} (J_{\text{p}})$	Electron (hole) current density in the bulk of the semiconductor, function of position	eqs 26–27
$k$	Boltzmann's constant	$1.38 \times 10^{-23} \text{ J K}^{-1}$
$k_{\text{c,max}}$	Rate constant for interfacial charge transfer	$10^{-18} \text{ cm}^4 \text{ s}^{-1} \leq k_{\text{c,max}} = k_{\text{v,max}} \leq 10^{-13} \text{ cm}^4 \text{ s}^{-1}$
$(k_{\text{v,max}})$	from the conduction (valence) band at optimal exoergicity	
$k_{\text{ct}}$	Rate constant for heterogeneous charge transfer across a semiconductor/liquid interface	(in units of $\text{cm}^4 \text{ s}^{-1}$ )
$k_{\text{ct,max}}$	Maximum observed rate constant for heterogeneous charge transfer across a semiconductor/liquid interface	(in units of $\text{cm}^4 \text{ s}^{-1}$ )
$k_{\text{et}} (k_{\text{ht}})$	Electron (hole) interfacial charge-transfer rate constant	eqs 5–6
$k_{\text{n}} (k_{\text{p}})$	Electron (hole) capture coefficient for traps	$k_{\text{n}} = k_{\text{p}} = 10^{-8} \text{ cm}^3 \text{ s}^{-1}$ $k_{\text{n,s}} = k_{\text{p,s}} = 10^{-8} \text{ cm}^3 \text{ s}^{-1}$ $2 \times 10^{-10} \text{ cm}^{-3} \text{ s}^{-1}$
$k_{\text{r}}$	Radiative recombination rate constant for InP	$0.5 \text{ eV}$
$\lambda$	Reorganization energy of the redox couple	(in units of $\text{cm}^{-3}$ )
$n (p)$	Concentration of electrons (holes) in the semiconductor, function of position	eq 8
$n_1 (p_1)$	Concentration of electrons (holes) in the conduction (valence) band when the trap energy is at the Fermi energy	
$n_{\text{i}}$	Intrinsic electron concentration of the undoped InP semiconductor	$1.5 \times 10^7 \text{ cm}^{-3}$
$n_{\text{o}} (p_{\text{o}})$	Concentration of electrons (holes) in the bulk of the solid in the dark at equilibrium	$n_{\text{o}} = 5 \times 10^{15} \text{ cm}^{-3}$ $p_{\text{o}} = 4.5 \times 10^{-2} \text{ cm}^{-3}$ $N_{\text{t}} = 10^{15} \text{ cm}^{-3}$ $10^9 \text{ cm}^{-2} \leq N_{\text{t,s}} \leq 10^{15} \text{ cm}^{-2}$ $N_{\text{v}} = 1.8 \times 10^{19} \text{ cm}^{-3}$ $N_{\text{c}} = 5.5 \times 10^{17} \text{ cm}^{-3}$ $p_{\text{i}}/n_{\text{o}} = 10^{-6}, 0.5, 2, \text{ and } 10$
$N_{\text{t}} (N_{\text{t,s}})$	Concentration of bulk (surface) traps	
$N_{\text{v}} (N_{\text{c}})$	Effective density of states in the valence (conduction) band	
$p_{\text{i}}$	Average excess minority carrier density created by the excitation pulse within a sample depth of $\alpha^{-1}$	
$\Delta p (\Delta n)$	Optically induced excess minority (majority) carrier concentration, function of position	(in units of $\text{cm}^{-3}$ )
$\Delta p_{\text{o}} (\Delta n_{\text{o}})$	Optically induced excess minority (majority) carrier concentration directly after excitation ( $t = 0$ ), function of position	(in units of $\text{cm}^{-3}$ )
$q$	Elementary charge	$1.60 \times 10^{-19} \text{ C}$
$R$	Total recombination rate associated with all recombination processes other than trap-mediated processes	eqs 19, 20
$R_{\text{r}}$	Radiative recombination rate	eq 34
$R_{\text{SRH}}$	Rate of Shockley–Read–Hall (SRH) nonradiative recombination in the semiconductor	eq 12
$\sigma$	Capture cross section for carriers by trap states	(in units of $\text{cm}^2$ )
$\sigma_{\text{n}} (\sigma_{\text{p}})$	Capture cross section for electrons (holes) by trap states	(in units of $\text{cm}^2$ )
$S_{\text{h}}$	High-level surface recombination velocity (in units of $\text{cm s}^{-1}$ )	$S_{\text{p}}S_{\text{h}}/(S_{\text{p}} + S_{\text{n}})$
$S_{\text{min}}$	Effective minority carrier capture velocity	
$S_{\text{n}} (S_{\text{p}} \equiv S_{\text{i}})$	Low-level surface recombination velocity for electrons (holes)	$S_{\text{n}} = N_{\text{t,s}}k_{\text{n,s}}, S_{\text{p}} = N_{\text{t,s}}k_{\text{p,s}}$ $10 \text{ cm s}^{-1} \leq S_{\text{p}} = S_{\text{n}} \leq 10^7 \text{ cm s}^{-1}$
$\tau$	Effective lifetime	eq 38
$\tau_{0,\text{n}} (\tau_{0,\text{p}})$	Low-level bulk SRH lifetime for electrons (holes)	$\tau_{0,\text{n}} = N_{\text{t}}k_{\text{n}} = 100 \text{ ns}$ $\tau_{0,\text{n}} = N_{\text{t}}k_{\text{n}} = 100 \text{ ns}$
$\tau_1$ & $(\tau_2)$	Decay times of the biexponential fit of a photoluminescence decay	eq 29
$\langle \tau \rangle$	Weighted lifetime parameter of a photoluminescence decay curve	eq 30
$\tau_{\text{h}}$	High-level bulk SRH lifetime	$\tau_{0,\text{n}} + \tau_{0,\text{p}} = 200 \text{ ns}$
$\tau_{\text{r,h}}$	High-injection radiative lifetime for this system	eq 41
$\tau_{\text{r,l}}$	Low-injection radiative lifetime for this system	$1000 \text{ ns}$ (eq 39)
$\tau_{\text{S,h}}$	High-level SRH lifetime associated with surface recombination	$\tau_{\text{S,h}} = 2\tau_{\text{S,l}}$
$\tau_{\text{S,l}}$	Low-level SRH lifetime associated with surface recombination	eq 42
$T$	System temperature	$300 \text{ K}$
$U$	Electrostatic potential in the semiconductor	eq 18
$v$	Thermal velocity for carriers	(in units of $\text{cm s}^{-1}$ )
$v_{\text{n}} (v_{\text{p}})$	Thermal velocity for electrons (holes)	(in units of $\text{cm s}^{-1}$ )
$v_{\text{sat,n}}$	Saturation velocity for electrons (holes) in the presence of large electric fields	$v_{\text{sat,n}} = 8.5 \times 10^6 \text{ cm s}^{-1}$ , eq 28
$(v_{\text{sat,p}})$		$v_{\text{sat,p}} = \text{not set}$
$V_{\text{bi}}$	Built-in potential	$0.123 \text{ eV}$
$\mu_{\text{n}} (\mu_{\text{p}})$	Mobility of electrons (holes) in the presence of an electric field	eq 28
$\mu_{0,\text{n}} (\mu_{0,\text{p}})$	Mobility of electrons (holes) in the absence of an electric field	$\mu_{0,\text{n}} = 3600 \text{ cm}^2 \text{ V}^{-1} \text{ s}^{-1}$ , eq 28 $\mu_{0,\text{p}} = 150 \text{ cm}^2 \text{ V}^{-1} \text{ s}^{-1}$



cerning the field dependence of photoexcited carrier dynamics can be drawn from photoluminescence decay data obtained under such conditions.

**Acknowledgment.** We acknowledge Reiner Nürnberg of the Weierstrass-Institut for his help with ToSCA and thank the U.S. Department of Energy, Office of Basic Energy Sciences, DE-FG-03-88ER13932, for support of this work. O.K. also acknowledges the Deutsche Forschungsgemeinschaft for a post-doctoral fellowship.

**Supporting Information Available:** (12 pages). Ordering information is given on any current masthead page.

## References and Notes

- (1) Gerischer, H. *J. Electroanal. Chem.* **1975**, *58*, 263.
- (2) Schmickler, W. *Interfacial Electrochemistry*; Oxford University Press: New York, 1996.
- (3) Lewis, N. S. *Annu. Rev. Phys. Chem.* **1991**, *42*, 543.
- (4) Memming, R. In *Electron-Transfer I*; Mattay, J., Ed.; Springer-Verlag: Berlin, 1994; Vol. 169; p 105.
- (5) Peter, L. M. *Chem. Rev.* **1990**, *90*, 753.
- (6) Fajardo, A. M.; Lewis, N. S. *Science* **1996**, *274*, 969.
- (7) Pomykal, K. E.; Fajardo, A. M.; Lewis, N. S. *J. Phys. Chem.* **1996**, *100*, 3652.
- (8) Pomykal, K. E.; Lewis, N. S. *J. Phys. Chem. B* **1997**, *101*, 2476.
- (9) Kesselman, J.; Hoffman, M. R.; Shreve, G. A.; Lewis, N. S. *J. Phys. Chem.* **1995**, *98*, 13385.
- (10) Gerischer, H. *J. Phys. Chem.* **1991**, *95*, 1356.
- (11) Gerischer, H.; Heller, A. *J. Electrochem. Soc.* **1992**, *139*, 113.
- (12) Fajardo, A. M.; Lewis, N. S. *J. Phys. Chem. B* **1997**, *101*, 11136.
- (13) Royea, W. J.; Fajardo, A. M.; Lewis, N. S. *J. Phys. Chem. B* **1997**, *101*, 11152.
- (14) Forbes, M. D. E.; Lewis, N. S. *J. Am. Chem. Soc.* **1990**, *112*, 3682.
- (15) Kumar, A.; Lewis, N. S. *J. Phys. Chem.* **1990**, *94*, 6002.
- (16) Horrocks, B. R.; Mirkin, M. V.; Bard, A. J. *J. Phys. Chem.* **1994**, *98*, 9106.
- (17) Uhlendorf, I.; Reineke-Koch, R.; Memming, R. *J. Phys. Chem.* **1996**, *100*, 4930.
- (18) Meier, A.; Kocha, S. S.; Hanna, M. C.; Nozik, A. J.; Siemoneit, K.; Reineke-Koch, R.; Memming, R. *J. Phys. Chem. B* **1997**, *101*, 7038.
- (19) Nozik, A. J.; Private communication.
- (20) Koval, C. A.; Howard, J. N. *Chem. Rev.* **1992**, *92*, 411.
- (21) Marcus, R. A. *J. Phys. Chem.* **1991**, *95*, 2010.
- (22) Marcus, R. A. *Electrochim. Acta* **1968**, *13*, 995.
- (23) Marcus, R. A.; Sutin, N. *Biochim. Biophys. Acta* **1985**, *811*, 265.
- (24) Smith, B. B.; Nozik, A. J. *Chem. Phys.* **1996**, *205*, 47.
- (25) Smith, B. B.; Nozik, A. J. In *19th D. O. E. Solar Photochemistry Research Conference*; Washington, D.C., 1995; p 103.
- (26) Rosenwaks, Y.; Thacker, B. R.; Ahrenkiel, R. K.; Nozik, A. J.; Yavneh, I. *Phys. Rev. B* **1994**, *50*, 1746.
- (27) Rosenwaks, Y.; Thacker, B. R.; Ahrenkiel, R. K.; Nozik, A. J. *J. Phys. Chem.* **1992**, *96*, 10096.
- (28) Bansal, A.; Tan, M. X.; Tufts, B. J.; Lewis, N. S. *J. Phys. Chem.* **1993**, *97*, 7309.
- (29) Nozik, A. J. Presented at the 211th National Meeting of the American Chemical Society, New Orleans LA, March 1996, Paper PHYS 11; 1996.
- (30) Rosenwaks, Y.; Thacker, B. R.; Nozik, A. J.; Ellingson, R. J.; Burr, K. C.; Tang, C. L. *J. Phys. Chem.* **1994**, *98*, 2739.
- (31) Rosenwaks, Y.; Nozik, A. J.; Yavneh, I. *J. Appl. Phys.* **1994**, *75*, 4255.
- (32) Nozik, A. J.; Parsons, C. A.; Dunlavy, D. J.; Keyes, B. M.; Ahrenkiel, R. K. *Solid State Commun.* **1990**, *75*, 297.
- (33) Krüger, O.; Jung, C.; Gajewski, H. *J. Phys. Chem.* **1994**, *98*, 12663.
- (34) Krüger, O.; Jung, C. *Ber. Bunsen-Ges. Phys. Chem.* **1994**, *98*, 1022.
- (35) Kenyon, C. N.; Ryba, G. N.; Lewis, N. S. *J. Phys. Chem.* **1993**, *97*, 12928.
- (36) Willig, F.; Bitterling, K.; Charlé, K.-P.; Decker, F. *Ber. Bunsen-Ges. Phys. Chem.* **1984**, *88*, 374.
- (37) van Roosbroeck, W. *Bell Syst. Technol. J.* **1950**, *29*, 560.
- (38) Gajewski, H. *GAMM (Ges. Angew. Math. Mechanik) Mitteilungen* **1993**, *16*, 35.
- (39) Gerischer, H. *J. Electrochem. Soc.* **1966**, *113*, 1174.
- (40) Ellis, A. B. In *Chemistry and Structure at Interfaces: New Laser and Optical Techniques*; Hall, R. B., Ellis, A. B., Eds.; VCH: Deerfield Beach, FL, 1986; p 245.
- (41) Hobson, W. S.; Ellis, A. B. *J. Appl. Phys.* **1983**, *54*, 5956.
- (42) Smandek, B.; Chmiel, G.; Gerischer, H. *Ber. Bunsen-Ges. Phys. Chem.* **1989**, *93*, 1094.
- (43) Hollingsworth, R. E.; Sites, J. R. *J. Appl. Phys.* **1982**, *53*, 5357.
- (44) Kauffman, J. F.; Richmond, G. L. *J. Appl. Phys.* **1993**, *73*, 1912.
- (45) Ramakrishna, S.; Rangarajan, S. K. *J. Electroanal. Chem.* **1991**, *308*, 49.
- (46) Ramakrishna, S.; Rangarajan, S. K. *J. Phys. Chem.* **1995**, *99*, 12631.
- (47) Tan, M. X.; Laibinis, P. E.; Nguyen, S. T.; Kesselman, J. M.; Stanton, C. E.; Lewis, N. S. *Prog. Inorg. Chem.* **1994**, *41*, 21.
- (48) Tan, M. X.; Kenyon, C. N.; Krüger, O.; Lewis, N. S. *J. Phys. Chem. B* **1997**, *101*, 2830.
- (49) Gajewski, H.; Glitzky, A.; Griepentrog, J.; Hünlich, R.; Kaiser, H.-C.; Rehberg, J.; Stephan, H.; Röpke, W.; Wenzel, H. Modellierung und Simulation von Bauelementen der Nano- und Optoelektronik. Weierstrass Institute for Applied Analysis and Stochastics, Mohrenstr. 39, D-10117 Berlin (Germany), 1996.
- (50) Krüger, O.; Kenyon, C. N.; Tan, M. X.; Lewis, N. S. *J. Phys. Chem. B* **1997**, *101*, 2840.
- (51) Krüger, O.; Jung, C.; Gajewski, H. *J. Phys. Chem.* **1994**, *98*, 12653.
- (52) Blakemore, J. S. *Semiconductor Statistics*; Dover Publications: New York, 1987.
- (53) Shockley, W.; Read, W. T. *Phys. Rev.* **1952**, *87*, 835.
- (54) Hall, R. N. *Phys. Rev.* **1952**, *87*, 387.
- (55) Bard, A. J.; Faulkner, L. R. *Electrochemical Methods: Fundamentals and Applications*; John Wiley & Sons: New York, 1980.
- (56) Sze, S. M. *The Physics of Semiconductor Devices*; 2nd ed.; Wiley: New York, 1981.
- (57) *Minority Carriers in III-V Semiconductors: Physics and Applications*; Ahrenkiel, R. K., Lundstrom, M. S., Eds.; Academic Press Inc.: San Diego, 1993; Vol. 39.
- (58) Many, A.; Goldstein, Y.; Grover, N. B. *Semiconductor Surfaces*; North-Holland Publishing Co.: New York, 1965.
- (59) Memming, R. *Ber. Bunsen-Ges. Phys. Chem.* **1987**, *91*, 353.
- (60) Ramakrishna, S.; Rangarajan, S. K. *J. Electroanal. Chem.* **1994**, *369*, 289.
- (61) Shreve, G. A.; Lewis, N. S. *J. Electrochem. Soc.* **1995**, *142*, 112.
- (62) Schroder, D. K. *Semiconductor Material and Device Characterization*; John Wiley & Sons: New York, 1990.
- (63) Krüger, O.; Jung, C. *Mater. Sci. Eng. B* **1993**, *20*, 232.
- (64) Ramakrishna, S.; Rangarajan, S. K. *J. Electroanal. Chem.* **1991**, *308*, 39.
- (65) Kauffman, J. F.; Balko, B. A.; Richmond, G. L. *J. Phys. Chem.* **1992**, *96*, 6371.
- (66) Fonash, S. J. *Solar Cell Device Physics*; Academic: New York, 1981.
- (67) Pankove, J. I. *Optical Processes in Semiconductors*; Dover Publications: New York, 1975.
- (68) Pierret, R. F. In *Modular Series on Solid State Devices*; Addison-Wesley Publishing Company: Reading, MA, 1988.
- (69) Gerischer, H. *Adv. Electrochem. Electrochem. Engr.* **1961**, *1*, 139.
- (70) Selberherr, S. *Analysis and Simulation of Semiconductor Devices*; Springer-Verlag: Wien, 1984.
- (71) Fischetti, M. V. *IEEE Trans. Electron Devices* **1991**, *38*, 634.
- (72) Yamaguchi, K.; Toyabe, T.; Koda, H. *Jpn. J. Appl. Phys.* **1975**, *14*, 1069.
- (73) Majerfeld, A.; Potter, K. E.; Robson, P. N. *J. Appl. Phys.* **1974**, *45*, 3681.
- (74) Windhorn, T. H.; Cook, L. W.; Haase, M. A.; Stillman, G. E. *Appl. Phys. Lett.* **1983**, *42*, 725.
- (75) Robson, P. N.; Potter, K. E.; Majerfeld, A. *IEEE Trans. Electron Devices* **1975**, *22*, 569.
- (76) Adachi, S. *Physical Properties of III-V Semiconductor Compounds*; John Wiley & Sons: New York, 1992; p 318.
- (77) Siegel, W.; Kühnel, G.; Koi, H.; Gerlach, W. *Phys. Status Solidi A* **1986**, *95*, 309.
- (78) Weaver, M. J.; Yee, E. L. *Inorg. Chem.* **1980**, *19*, 1936.
- (79) Tyagi, M. S.; Nijs, J. F.; Van Overstraeten, R. *J. Solid-State Electron.* **1982**, *25*, 411.
- (80) Shumaker, M. L.; Dollard, W. J.; Waldeck, D. H. *J. Phys. Chem.* **1992**, *96*, 10371.
- (81) Vaitkus, J. *Phys. Status Solidi* **1976**, *34*, 769.
- (82) Gottesfeld, S. *Ber. Bunsen-Ges. Phys. Chem.* **1987**, *91*, 362.
- (83) Rosenwaks, Y.; Shapira, Y.; Huppert, D. *Phys. Rev. B* **1992**, *45*, 9108.
- (84) Tan, M. X.; Kenyon, C. N.; Lewis, N. S. *J. Phys. Chem.* **1994**, *98*, 4959.
- (85) Ramakrishna, S.; Rangarajan, S. K. *J. Phys. Chem.* **1996**, *100*, 16365.
- (86) Boulou, M. B.; Bois, D. *J. Appl. Phys.* **1977**, *48*, 4713.